Kramer, S., Scawthorn, C. "Geotechnical Earthquake Considerations."
Bridge Engineering Handbook.
Ed. Wai-Fah Chen and Lian Duan
Boca Raton: CRC Press, 2000

Section IV

Seismic Design

33

Geotechnical Earthquake Considerations

Steven Kramer
University of Washington

Charles Scawthorn
EQE International

33.1 Introduction

Earthquakes are naturally occurring broad-banded vibratory ground motions, that are due to a number of causes including tectonic ground motions, volcanism, landslides, rockbursts, and man-made explosions, the most important of which are caused by the fracture and sliding of rock along tectonic **faults** within the Earth's crust. For most earthquakes, shaking and ground failure are the dominant and most widespread agents of damage. Shaking near the actual earthquake rupture lasts only during the time when the fault ruptures, a process which takes seconds or at most a few minutes. The seismic waves generated by the rupture propagate long after the movement on the fault has stopped, however, spanning the globe in about 20 min. Typically, earthquake ground

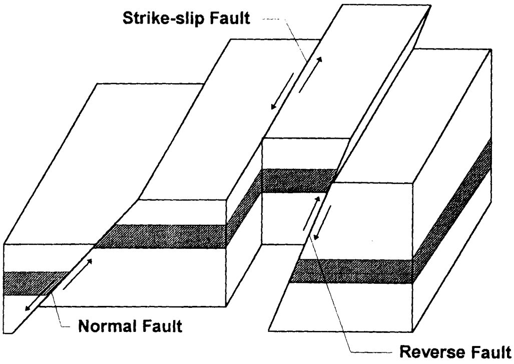

FIGURE 33.1 Fault types.

motions are powerful enough to cause damage only in the near field (i.e., within a few tens of kilometers from the causative fault) — in a few instances, long-period motions have caused significant damage at great distances, to selected lightly damped structures, such as in the 1985 Mexico City earthquake, where numerous collapses of mid- and high-rise buildings were due to a magnitude 8.1 earthquake occurring at a distance of approximately 400 km from Mexico City.

33.2 Seismology

Plate Tectonics: In a global sense, tectonic earthquakes result from motion between a number of large plates comprising the Earth's crust or lithosphere (about 15 in total). These plates are driven by the convective motion of the material in the Earth's mantle, which in turn is driven by heat generated at the Earth's core. Relative plate motion at the fault interface is constrained by friction and/or **asperities** (areas of interlocking due to protrusions in the fault surfaces). However, strain energy accumulates in the plates, eventually overcomes any resistance, and causes slip between the two sides of the fault. This sudden slip, termed **elastic rebound** by Reid [49] based on his studies of regional deformation following the 1906 San Francisco earthquake, releases large amounts of energy, which constitute the earthquake. The location of initial radiation of seismic waves (i.e., the first location of dynamic rupture) is termed the **hypocenter**, while the projection on the surface of the Earth directly above the hypocenter is termed the **epicenter**. Other terminology includes **near-field** (within one source dimension of the epicenter, where source dimension refers to the length of faulting), **far-field** (beyond near-field) and **meizoseismal** (the area of strong shaking and damage). Energy is radiated over a broad spectrum of frequencies through the Earth, in **body waves** and **surface waves** [4]. Body waves are of two types: P waves (transmitting energy via push–pull motion) and slower S waves (transmitting energy via shear action at right angles to the direction of motion). Surface waves are also of two types: horizontally oscillating **Love waves** (analogous to S body waves) and vertically oscillating **Rayleigh waves**.

Faults are typically classified according to their sense of motion, Figure 33.1. Basic terms include **transform** or **strike slip** (relative fault motion occurs in the horizontal plane, parallel to the strike of the fault), **dip-slip** (motion at right angles to the strike, up- or down-slip), **normal** (dip-slip motion, two sides in tension, move away from each other), **reverse** (dip-slip, two sides in compression, move toward each other), and **thrust** (low-angle reverse faulting).

Generally, earthquakes will be concentrated in the vicinity of faults; faults that are moving more rapidly than others will tend to have higher rates of seismicity, and larger faults are more likely than others to produce a large event. Many faults are identified on regional geologic maps, and useful information on fault location and displacement history is available from local and national geologic surveys in areas of high seismicity. An important development has been the growing recognition of **blind thrust faults**, which emerged as a result of the several earthquakes in the 1980s, none of which was accompanied by surface faulting [61].

33.3 Measurement of Earthquakes

Magnitude

An individual earthquake is a unique release of strain energy — quantification of this energy has formed the basis for measuring the earthquake event. C.F. Richter [51] was the first to define earthquake **magnitude**, as

$$M_L = \log \mathrm{A} - \log A_o \tag{33.1}$$

where M_L is **local magnitude** (which Richter only defined for Southern California), A is the maximum trace amplitude in microns recorded on a standard Wood–Anderson short-period torsion seismometer at a site 100 km from the epicenter, and log A_o is a standard value as a function of distance, for instruments located at distances other than 100 km and less than 600 km. A number of other magnitudes have since been defined, the most important of which are **surface wave** magnitude M_S, body wave magnitude m_b, and **moment magnitude** M_W. Magnitude can be related to the total energy in the expanding wave front generated by an earthquake, and thus to the total energy release — an empirical relation by Richter is

$$\log_{10} E_s = 11.8 + 1.5\, M_s \tag{33.2}$$

where $E_{S,}$ is the total energy in ergs. Due to the observation that deep-focus earthquakes commonly do not register measurable surface waves with periods near 20 s, a body wave magnitude m_b was defined [25], which can be related to M_S [16]:

$$m_b = 2.5 + 0.63 M_S \tag{33.3}$$

Body wave magnitudes are more commonly used in eastern North America, due to the deeper earthquakes there. More recently, **seismic moment** has been employed to define a moment magnitude M_W [26] (also denoted as bold-face **M**) which is finding increased and widespread use:

$$\mathrm{Log}\ M_o = 1.5\, M_W + 16.0 \tag{33.4}$$

where seismic moment M_o (dyne-cm) is defined as [33]

$$M_o = \mu A \bar{u} \tag{33.5}$$

where μ is the material shear modulus, A is the area of fault plane rupture, and $\bar{u}$ is the mean relative displacement between the two sides of the fault (the averaged fault slip). Comparatively, M_W and M_S are numerically almost identical up to magnitude 7.5. Figure 33.2 indicates the relationship between moment magnitude and various magnitude scales.

From the foregoing discussion, it can be seen that magnitude and energy are related to fault rupture length and slip. Slemmons [60] and Bonilla et al. [5] have determined statistical relations between these parameters, for worldwide and regional data sets, aggregated and segregated by type of faulting (normal, reverse, strike-slip). Bonilla et al.'s worldwide results for all types of faults are

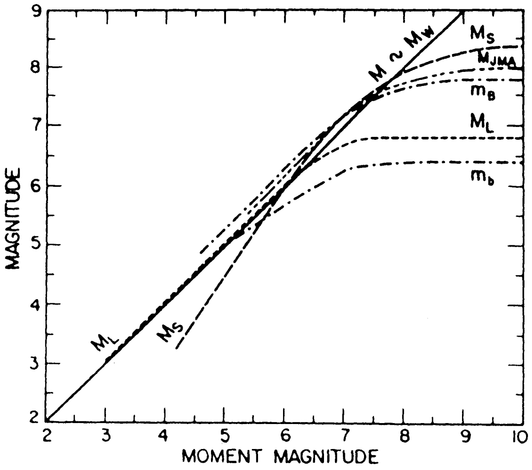

FIGURE 33.2 Relationship between moment magnitude and various magnitude scales. (*Source*: Campbell, K. W., *Earthquake Spectra,* 1(4), 759–804, 1985. With permission.)

$$M_s = 6.04 + 0.708 \log_{10} L \qquad s = 0.306 \tag{33.6}$$

$$\log_{10} L = -2.77 + 0.619 M_s \qquad s = 0.286 \tag{33.7}$$

$$M_s = 6.95 + 0.723 \log_{10} d \qquad s = 0.323 \tag{33.8}$$

$$\log_{10} d = -3.58 + 0.550 M_s \qquad s = 0.282 \tag{33.9}$$

which indicates, for example, that, for $M_S = 7$, the average fault rupture length is about 36 km (and the average displacement is about 1.86 m). Conversely, a fault of 100 km length is capable of about an $M_S = 7.5$* event (see also Wells and Coppersmith [66] for alternative relations).

Intensity

In general, seismic intensity is a metric of the effect, or the strength, of an earthquake hazard at a specific location. While the term can be generically applied to engineering measures such as peak ground acceleration, it is usually reserved for qualitative measures of location-specific earthquake effects, based on observed human behavior and structural damage. Numerous intensity scales were developed in preinstrumental times — the most common in use today are the Modified Mercalli (MMI) [68] (Table 33.1), the Rossi–Forel (R-F), the Medvedev-Sponheur-Karnik (MSK-64, 1981), and the Japan Meteorological Agency (JMA) scales.

Time History

Sensitive strong motion seismometers have been available since the 1930s, and they record actual ground motions specific to their location, Figure 33.3. Typically, the ground motion records, termed **seismographs** or **time histories**, have recorded acceleration (these records are termed **accelerograms**), for

---

*Note that $L = g(M_S)$ should not be inverted to solve for $M_S = f(L)$, as a regression for $y = f(x)$ is different from a regression for $x = g(y)$.

TABLE 33.1 Modified Mercalli Intensity Scale of 1931

I	Not felt except by a very few under especially favorable circumstances
II	Felt only by a few persons at rest, especially on upper floors of buildings. Delicately suspended objects may swing.
III	Felt quite noticeably indoors, especially on upper floors of buildings, but many people do not recognize it as an earthquake; standing automobiles may rock slightly; vibration like passing truck; duration estimated
IV	During the day felt indoors by many, outdoors by few; at night some awakened; dishes, windows, and doors disturbed; walls make creaking sound; sensation like heavy truck striking building; standing automobiles rock noticeably
V	Felt by nearly everyone; many awakened; some dishes, windows, etc., broken; a few instances of cracked plaster; unstable objects overturned; disturbance of trees, poles, and other tall objects sometimes noticed; pendulum clocks may stop
VI	Felt by all; many frightened and run outdoors; some heavy furniture moved; a few instances of fallen plaster or damaged chimneys; damage slight
VII	Everybody runs outdoors; damage negligible in buildings of good design and construction, slight to moderate in well-built ordinary structures; considerable in poorly built or badly designed structures; some chimneys broken; noticed by persons driving automobiles
VIII	Damage slight in specially designed structures, considerable in ordinary substantial buildings, with partial collapse, great in poorly built structures; panel walls thrown out of frame structures; fall of chimneys, factory stacks, columns, monuments, walls; heavy furniture overturned; sand and mud ejected in small amounts; changes in well water; persons driving automobiles disturbed
IX	Damage considerable in specially designed structures; well-designed frame structures thrown out of plumb; great in substantial buildings, with partial collapse; buildings shifted off foundations; ground cracked conspicuously; underground pipes broken
X	Some well-built wooden structures destroyed; most masonry and frame structures destroyed with foundations; ground badly cracked; rails bent; landslides considerable from river banks and steep slopes; shifted sand and mud; water splashed over banks
XI	Few, if any (masonry) structures remain standing; bridges destroyed; broad fissures in ground; underground pipelines completely out of service; earth slumps and land slips in soft ground; rails bent greatly
XII	Damage total; waves seen on ground surfaces; lines of sight and level distorted; objects thrown upward into the air

After Wood and Neumann [68].

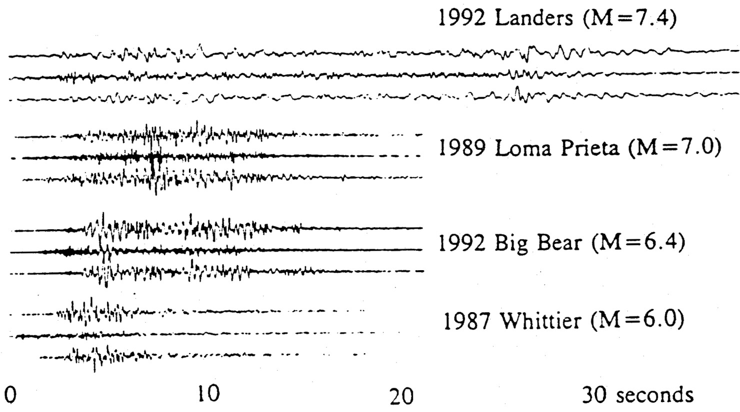

FIGURE 33.3 Typical earthquake accelerograms. (Courtesy of Darragh et al., 1994.)

many years in analog form on photographic film and, more recently, digitally. Analog records required considerable effort for correction due to instrumental drift, before they could be used.

Time histories theoretically contain complete information about the motion at the instrumental location, recording three *traces* or orthogonal records (two horizontal and one vertical). Time histories (i.e., the earthquake motion at the site) can differ dramatically in duration, frequency, content, and amplitude. The maximum amplitude of recorded acceleration is termed the **peak ground acceleration**, PGA (also termed the ZPA, or **zero period acceleration**); peak ground velocity

(PGV) and peak ground displacement (PGD) are the maximum respective amplitudes of velocity and displacement. Acceleration is normally recorded, with velocity and displacement being determined by integration; however, velocity and displacement meters are deployed to a lesser extent. Acceleration can be expressed in units of cm/s^2 (termed *gals*), but is often also expressed in terms of the fraction or percent of the acceleration of gravity (980.66 gals, termed 1 *g*). Velocity is expressed in cm/s (termed *kine*). Recent earthquakes — 1994 Northridge, M_W 6.7 and 1995 Hanshin (Kobe) M_W 6.9 — have recorded PGAs of about 0.8 *g* and PGVs of about 100 kine, while almost 2 g was recorded in the 1992 Cape Mendocino earthquake.

Elastic Response Spectra

If a single-degree-of-freedom (SDOF) mass is subjected to a time history of ground (i.e., base) motion similar to that shown in Figure 33.3, the mass or elastic **structural response** can be readily calculated as a function of time, generating a **structural response time history**, as shown in Figure 33.4 for several oscillators with differing natural periods. The response time history can be calculated by direct integration of Eq. (33.1) in the **time domain**, or by solution of the **Duhamel** integral. However, this is time-consuming, and the elastic response is more typically calculated in the **frequency domain** [12].

For design purposes, it is often sufficient to know only the maximum amplitude of the response time history. If the natural period of the SDOF is varied across a spectrum of engineering interest (typically, for natural periods from 0.03 to 3 or more seconds, or frequencies of 0.3 to 30+ Hz), then the plot of these maximum amplitudes is termed a **response spectrum**. Figure 33.4 illustrates this process, resulting in S_d, the *displacement response spectrum*, while Figure 33.5 shows (a) the S_d, displacement response spectrum, (b) S_v, the *velocity response spectrum* (also denoted PSV, the pseudo-spectral velocity, "pseudo" to emphasize that this spectrum is not exactly the same as the relative velocity response spectrum), and (c) S_a, the *acceleration response spectrum*. Note that

$$S_v = \frac{2\pi}{T} S_d = \varpi S_d \tag{33.10}$$

and

$$S_a = \frac{2\pi}{T} S_v = \varpi S_v = \left(\frac{2\pi}{T}\right)^2 S_d = \varpi^2 S_d \tag{33.11}$$

Response spectra form the basis for much modern earthquake engineering structural analysis and design. They are readily calculated *if* the ground motion is known. For design purposes, however, response spectra must be estimated — this process is discussed below. Response spectra may be plotted in any of several ways, as shown in Figure 33.5 with arithmetic axes, and in Figure 33.6, where the velocity response spectrum is plotted on tripartite logarithmic axes, which equally enables reading of displacement and acceleration response. Response spectra are most normally presented for 5% of critical damping.

Inelastic Response Spectra

While the foregoing discussion has been for elastic response spectra, most structures are not expected, or even designed, to remain elastic under strong ground motions. Rather, structures are expected to enter the *inelastic* region — the extent to which they behave inelastically can be defined by the **ductility factor**, μ:

$$\mu = \frac{u_m}{u_y} \tag{33.12}$$

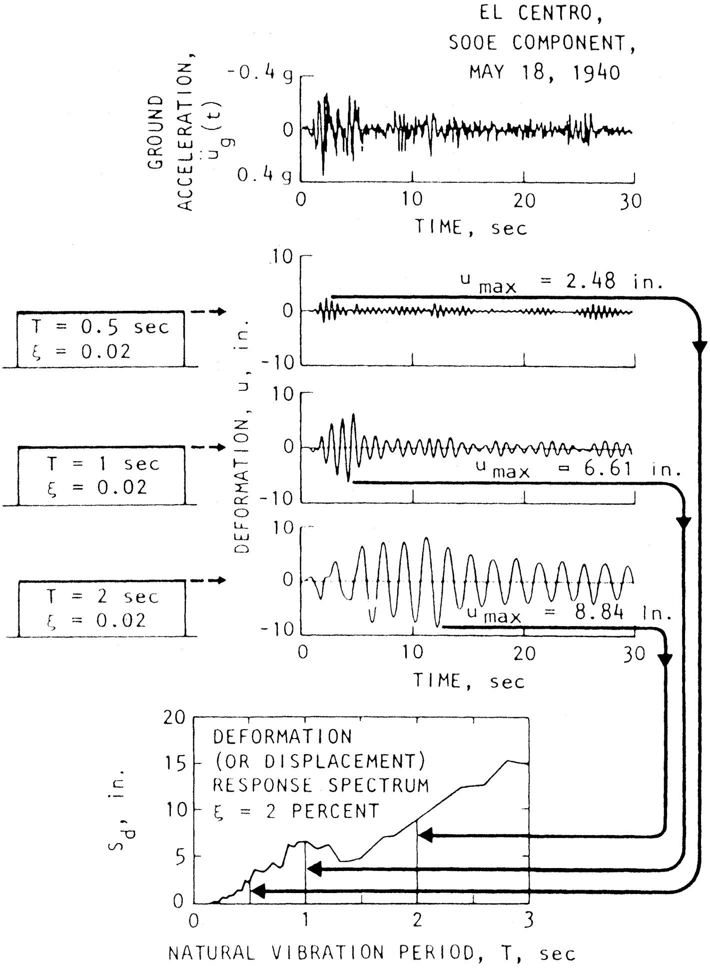

FIGURE 33.4 Computation of deformation (or displacement) response spectrum. (*Source*: Chopra, A. K., *Dynamics of Structures, A Primer,* Earthquake Engineering Research Institute, Oakland, CA, 1981. With permission.)

where u_m is the actual displacement of the mass under actual ground motions, and u_y is the displacement at yield (i.e., that displacement which defines the extreme of elastic behavior). Inelastic response spectra can be calculated in the time domain by direct integration, analogous to elastic response spectra but with the structural stiffness as a nonlinear function of displacement, $k = k(u)$. If elastoplastic behavior is assumed, then elastic response spectra can be readily modified to reflect inelastic behavior, on the basis that (1) at low frequencies (<0.3 Hz) displacements are the same, (2) at high frequencies (>33 Hz), accelerations are equal, and (3) at intermediate frequencies, the absorbed energy is preserved. Actual construction of inelastic response spectra on this basis is shown in Figure 33.9, where $DVAA_0$ is the elastic spectrum, which is reduced to D' and V' by the ratio of $1/\mu$ for frequencies less than 2 Hz, and by the ratio of $1/(2\mu - 1)^{1/2}$ between 2 and 8 Hz. Above 33 Hz, there is no reduction. The result is the inelastic acceleration spectrum ($D'V'A'A_0$), while $A''A_0'$ is the inelastic displacement spectrum. A specific example, for ZPA = 0.16 g, damping = 5% of critical and $\mu = 3$ is shown in Figure 33.10.

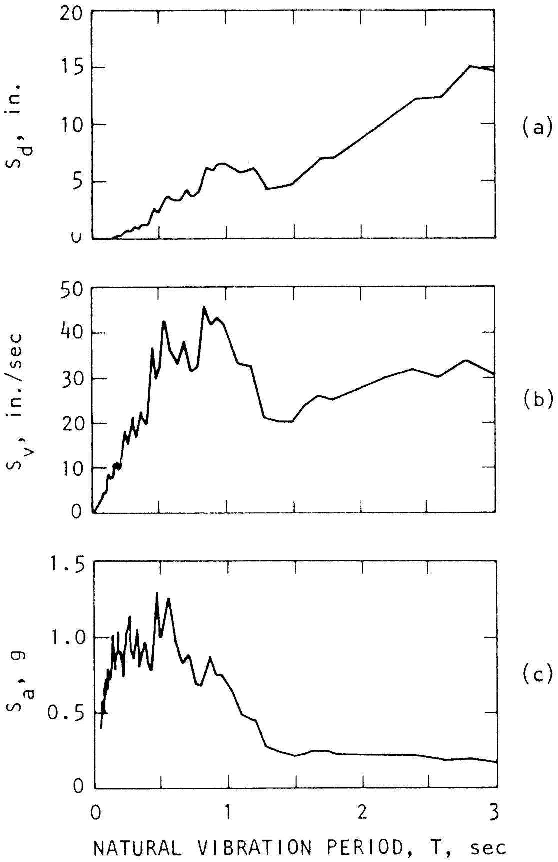

FIGURE 33.5 Response spectra. (*Source*: Chopra, A. K., *Dynamics of Structures, A Primer,* Earthquake Engineering Research Institute, Oakland, CA, 1981. With permission.)

33.4 Strong Motion Attenuation and Duration

The rate at which earthquake ground motion decreases with distance, termed **attenuation**, is a function of the regional geology and inherent characteristics of the earthquake and its source. Campbell [10] offers an excellent review of North American relations up to 1985. Initial relationships were for PGA, but regression of the amplitudes of response spectra at various periods is now common, including consideration of fault type and effects of soil. A currently favored relationship is

Campbell and Bozorgnia [11] (PGA — Worldwide Data)

$$\begin{aligned}\ln(\mathrm{PGA}) = {} & -3.512 + 0.904M - 1.328\ln\sqrt{\left\{R_s^2 + \left[0.149\exp(0.647M)\right]^2\right\}} \\ & + \left[1.125 - 0.112\ln\left(R_s\right) - 0.0957M\right]F \qquad (33.13 \\ & + \left[0.440 - 0.171\ln\left(R_s\right)\right]S_{sr} + \left[0.405 - 0.222\ln\left(R_s\right)\right]S_{hr} + \varepsilon\end{aligned}$$

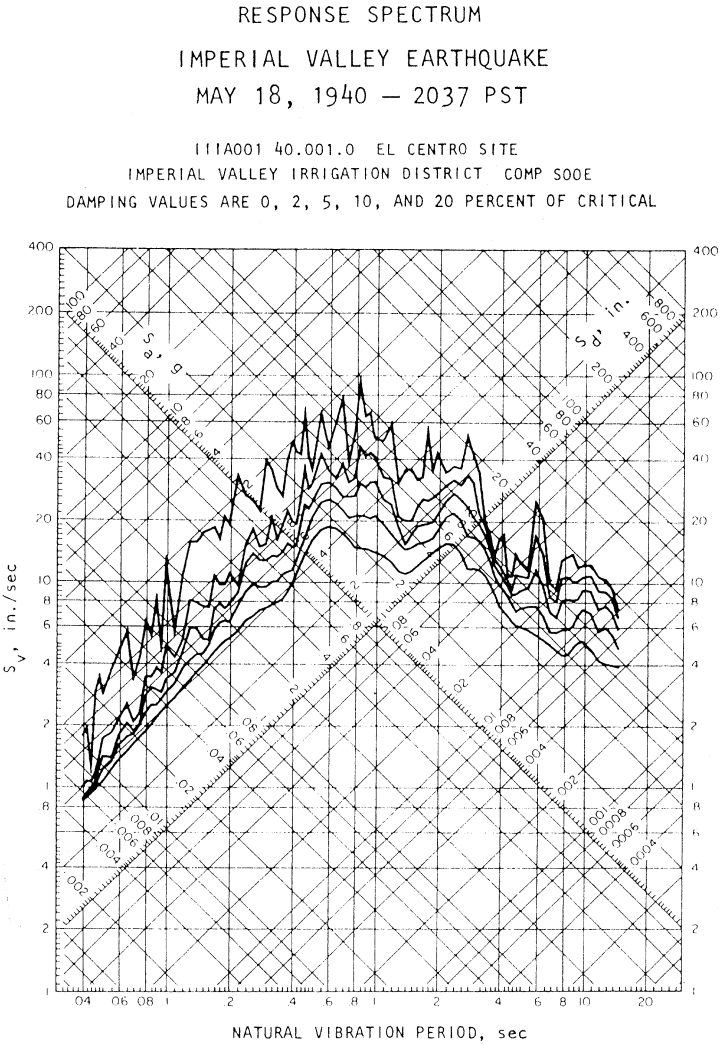

FIGURE 33.6 Response spectra, tripartite plot (El Centro S 0° E component). (*Source*: Chopra, A. K., *Dynamics of Structures, A Primer,* Earthquake Engineering Research Institute, Oakland, CA, 1981. With permission.)

where

PGA = the geometric mean of the two horizontal components of peak ground acceleration (g)
M = moment magnitude (M_w)
R_s = the closest distance to seismogenic rupture on the fault (km)
F = 0 for strike-slip and normal faulting earthquakes, and 1 for reverse, reverse-oblique, and thrust faulting earthquakes
S_{sr} = 1 for soft-rock sites
S_{hr} = 1 for hard-rock sites
$S_{sr} = S_{hr} =$ 0 for alluvium sites
ε = is a random error term with zero mean and standard deviation equal to $\sigma_{\ln}$(PGA), the standard error of estimate of ln(PGA)

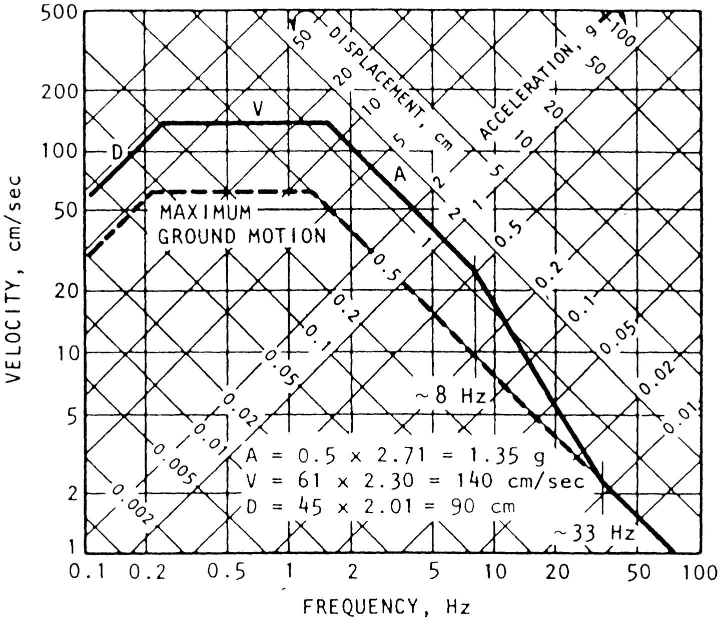

FIGURE 33.7 Idealized elastic design spectrum, horizontal motion (ZPA = 0.5 *g*, 5% damping, one sigma cumulative probability. (*Source*: Newmark, N. M. and Hall, W. J., *Earthquake Spectra and Design,* Earthquake Engineering Research Institute, Oakland, CA, 1982. With permission.)

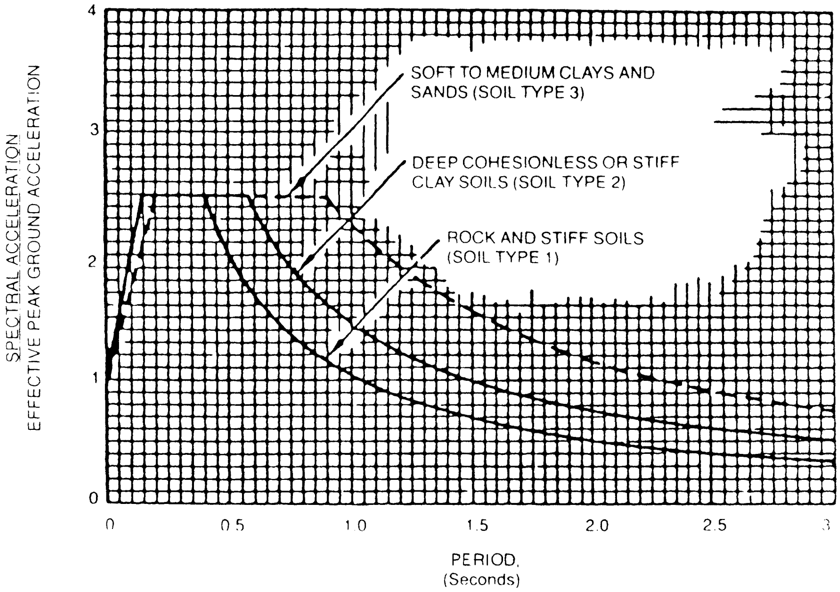

FIGURE 33.8 Normalized response spectra shapes. (*Source*: Uniform Building Code, Structural Engineering Design Provisions, Vol. 2, Intl. Conf. Building Officials, Whittier, 1994. With permission.)

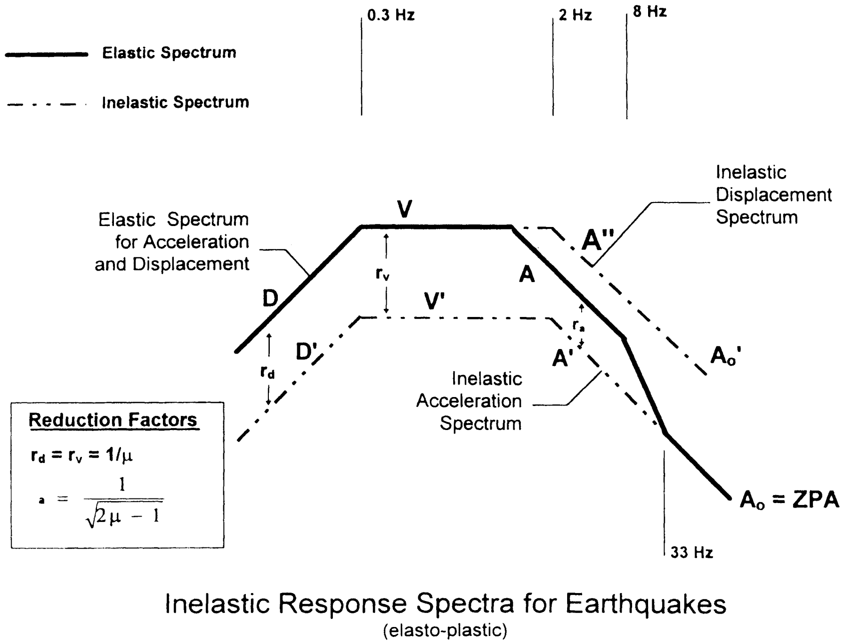

FIGURE 33.9 Inelastic response spectra for earthquakes. (*Source*: Newmark, N. M. and Hall, W. J., *Earthquake Spectra and Design,* Earthquake Engineering Research Institute, Oakland, CA, 1982.)

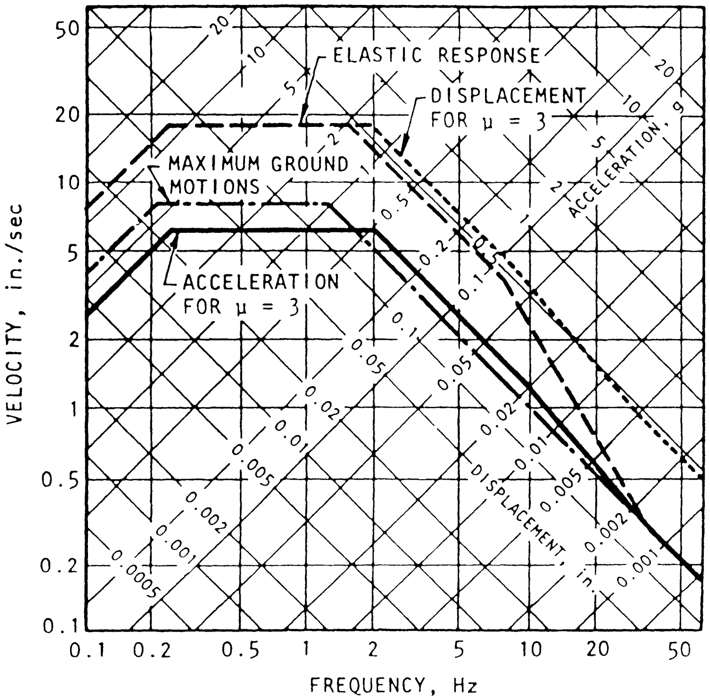

FIGURE 33.10 Example inelastic response spectra. (*Source*: Newmark, N. M. and Hall, W. J., *Earthquake Spectra and Design,* Earthquake Engineering Research Institute, Oakland, CA, 1982.)

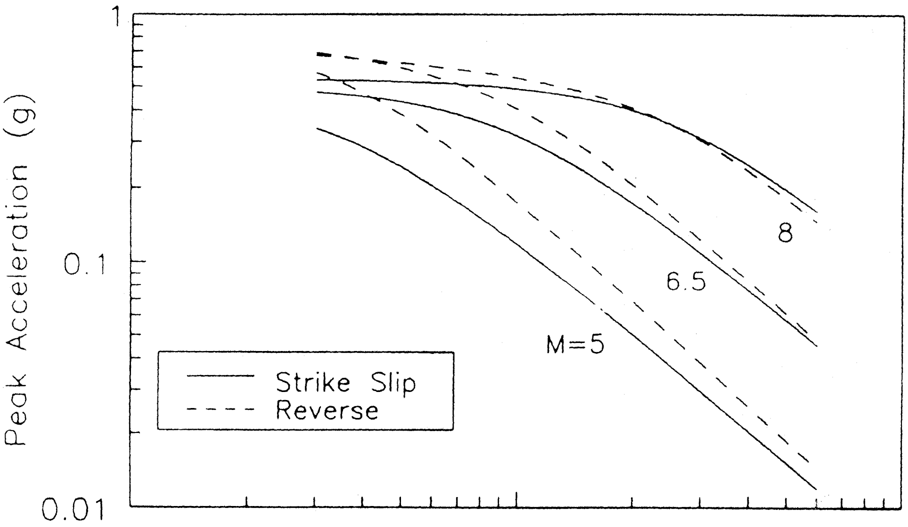

FIGURE 33.11 Campbell and Bozorgnia worldwide attenuation relationship showing (for alluvium) the scaling of peak horizontal acceleration with magnitude and style of faulting. (*Source*: Campbell, K. W. and Bozorgnia, Y., in *Proc. Fifth U.S. National Conference on Earthquake Engineering,* Earthquake Engineering Research Institute, Oakland, CA, 1994. With permission.)

Regarding the uncertainty, ε was estimated as

$$\sigma_{\ln}(\mathrm{PGA}) = \left| \begin{array}{ll} 0.55 & \text{if PGA } < 0.068 \\ 0.173 - 0.140 \ln(\mathrm{PGA}) & \text{if } 0.068 \leq \text{ PGA } \leq 0.21 \\ 0.39 & \text{if PGA } > 0.21 \end{array} \right.$$

Figure 33.11 indicates, for alluvium, median values of the attenuation of peak horizontal acceleration with magnitude and style of faulting. Many other relationships are also employed (e.g., Boore et al.[6]).

33.5 Probabilistic Seismic Hazard Analysis

The probabilistic seismic hazard analysis (PSHA) approach entered general practice with Cornell's [13] seminal paper, and basically employs the theorem of total probability to formulate:

$$P(Y) = \sum_F \sum_M \sum_R p(Y|M, R)p(M)p(R) \tag{33.14}$$

where
Y = a measure of intensity, such as PGA, response spectral parameters PSV, etc.
$p(Y|M,R)$ = the probability of Y given earthquake magnitude M and distance R (i.e., attenuation)
$p(M)$ = the probability of a given earthquake magnitude M
$p(R)$ = the probability of a given distance R, and
F = seismic sources, whether discrete such as faults, or distributed

This process is illustrated in Figure 33.12, where various seismic sources (faults modeled as line sources and dipping planes, and various distributed or area sources, including a background source to account for miscellaneous seismicity) are identified, and their seismicity characterized on the basis of historic seismicity and/or geologic data. The effects at a specific site are quantified on the

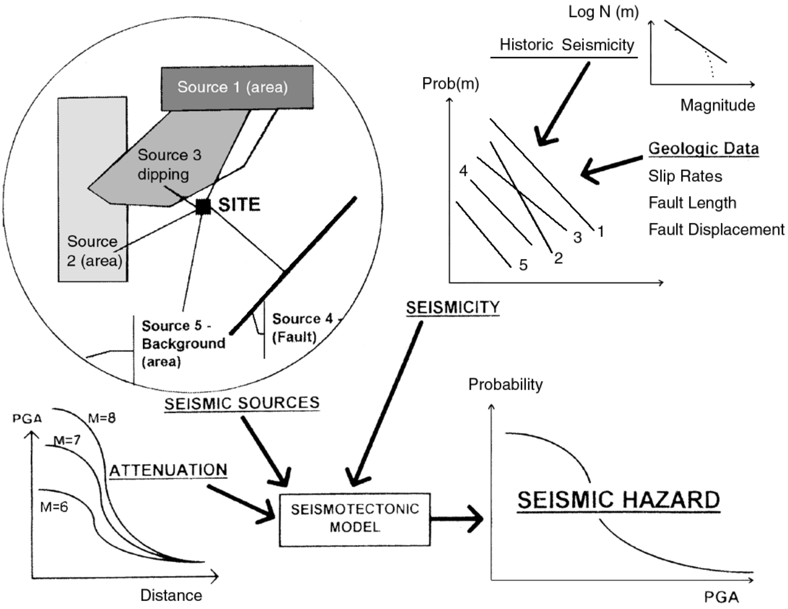

FIGURE 33.12 Elements of seismic hazard analysis — seismotectonic model is composed of seismic sources, whose seismicity is characterized on the basis of historic seismicity and geologic data, and whose effects are quantified at the site via strong motion attenuation models.

basis of strong ground motion modeling, also termed attenuation. These elements collectively are the **seismotectonic model** — their integration results in the **seismic hazard**.

There is an extensive literature on this subject [42,50] so that only key points will be discussed here. Summation is indicated, as integration requires closed-form solutions, which are usually precluded by the empirical form of the attenuation relations. The $p(Y|M,R)$ term represents the full probabilistic distribution of the attenuation relation — summation must occur over the full distribution, due to the significant uncertainty in attenuation. The $p(M)$ term is referred to as the **magnitude–frequency relation**, which was first characterized by Gutenberg and Richter [24] as

$$\log \mathbf{N}(m) = a_N - b_N m \tag{33.15}$$

where $\mathbf{N}(m)$ = the number of earthquake events equal to or greater than magnitude m occurring on a seismic source per unit time, and a_N and b_N are regional constants (10^{a_N} = the total number of earthquakes with magnitude >0, and b_N is the rate of seismicity; b_N is typically 1 ± 0.3). The Gutenberg–Richter relation can be normalized to

$$\mathbf{F}(m) = 1. - \exp\,[-\,\mathbf{B}_M\,(m - \mathbf{M}_{\mathrm{o})}] \tag{33.16}$$

where $F(m)$ is the cumulative distribution function (CDF) of magnitude, $\mathbf{B}_M$ is a regional constant and $\mathbf{M}_{\mathrm{o}}$ is a small enough magnitude such that lesser events can be ignored. Combining this with a Poisson distribution to model large earthquake occurrence [20] leads to the CDF of earthquake magnitude per unit time

$$\boldsymbol{F}(m) = \exp\,[-\exp\,\{-\,a_M\,(m - \mu_M)\}] \tag{33.17}$$

which has the form of a Gumbel [23] extreme value type I (largest values) distribution (denoted $\mathrm{EX}_{\mathrm{I,L}}$), which is an unbounded distribution (i.e., the variate can assume any value). The parameters

a_M and μ_M can be evaluated by a least-squares regression on historical seismicity data, although the probability of very large earthquakes tends to be overestimated. Several attempts have been made to account for this (e.g., Cornell and Merz [14]). Yegulalp and Kuo [70] have used Gumbel's Type III (largest value, denoted $\mathrm{EX}_{\mathrm{III,L}}$) to successfully account for this deficiency. This distribution

$$F(m) = \exp\left[-\left(\frac{w-m}{w-u}\right)^k\right] \tag{33.18}$$

has the advantage that w is the largest possible value of the variate (i.e., earthquake magnitude), thus permitting (when w, u, and k are estimated by regression on historical data) an estimate of the source's largest possible magnitude. It can be shown (Yegulalp and Kuo [70]) that estimators of w, u, and k can be obtained by satisfying Kuhn–Tucker conditions although, if the data is too incomplete, the $\mathrm{EX}_{\mathrm{III,L}}$ parameters approach those of the $\mathrm{EX}_{\mathrm{I,L}}$. Determination of these parameters requires careful analysis of historical seismicity data (which is highly complex and something of an art [17], and the merging of the resulting statistics with estimates of maximum magnitude and seismicity made on the basis of geologic evidence (i.e., as discussed above, maximum magnitude can be estimated from fault length, fault displacement data, time since last event, and other evidence, and seismicity can be estimated from fault slippage rates combined with time since the last event, see Schwartz [55] for an excellent discussion of these aspects). In a full probabilistic seismic hazard analysis, many of these aspects are treated fully or partially probabilistically, including the attenuation, magnitude–frequency relation, upper- and lower-bound magnitudes for each source zone, geographic bounds of source zones, fault rupture length, and many other aspects. The full treatment requires complex specialized computer codes, which incorporate uncertainty via use of multiple alternative source zonations, attenuation relations, and other parameters [3,19] often using a logic tree format. A number of codes have been developed using the public domain FRISK (Fault RISK) code first developed by McGuire [37].

33.6 Site Response

When seismic waves reach a site, the ground motions they produce are affected by the geometry and properties of the geologic materials at that site. At most bridge sites, rock will be covered by some thickness of soil which can markedly influence the nature of the motions transmitted to the bridge structure as well as the loading on the bridge foundation. The influence of local site conditions on ground response has been observed in many past earthquakes, but specific provisions for site effects were not incorporated in codes until 1976.

The manner in which a site responds during an earthquake depends on the near-surface stiffness gradient and on how the incoming waves are reflected and refracted by the near-surface materials. The interaction between seismic waves and near-surface materials can be complex, particularly when surface topography and/or subsurface stratigraphy is complex. Quantification of site response has generally been accomplished by analytical or empirical methods.

Basic Concepts

The simplest possible case of site response would consist of a uniform layer of viscoelastic soil of density, ρ, shear modulus, G, viscosity, η, and thickness, H, resting on rigid bedrock and subjected to vertically propagating shear waves (Figure 33.13a). The response of the layer would be governed by the wave equation

$$\rho \frac{\partial^2 u}{\partial t^2} = G \frac{\partial^2 u}{\partial z^2} + \eta \frac{\partial^3 u}{\partial z^2 \partial t} \tag{33.19}$$

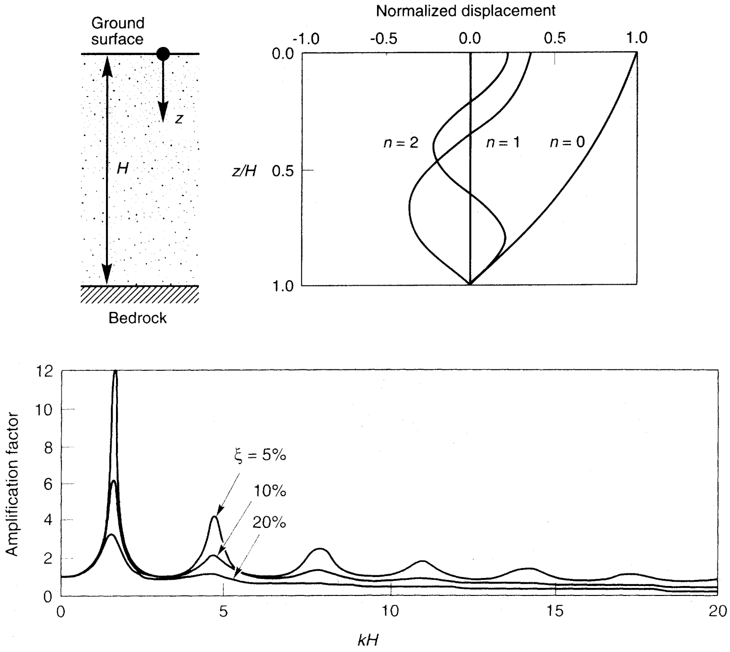

FIGURE 33.13 Illustration of (top) mode shapes and (bottom) amplification function for uniform elastic layer underlain by rigid boundary. (*Source*: Kramer, S.L., *Geotechnical Earthquake Engineering*, Prentice-Hall, Upper Saddle River, NJ, 1996.)

which has a solution that can be expressed in the form of upward and downward traveling waves. At certain frequencies, these waves interfere constructively to produce increased amplitudes; at other frequencies, the upward and downward traveling waves tend to cancel each other and produce lower amplitudes. Such a system can easily be shown to have an infinite number of natural frequencies and mode shapes (Figure 33.13 (top)) given by

$$\omega_n = \frac{v_s}{H}\left(\frac{\pi}{2} + n\pi\right) \quad \text{and} \quad \phi_n = \cos\left[\frac{z}{H}\left(\frac{\pi}{2} + n\pi\right)\right] \tag{33.20}$$

Note that the fundamental, or characteristic site period, is given by $T_s = 2\pi/\omega_o = 4H/v_s$. The ratio of ground surface to bedrock amplitude can be expressed in the form of an **amplification function** as

$$A(\omega) = \frac{1}{\sqrt{\cos^2\left(\omega H / v_s + \left[\xi\left(\omega H / v_S\right)\right]^2\right)}} \tag{33.21}$$

Figure 33.13(b) shows the amplification function which illustrates the frequency-dependent nature of site amplification. The amplification factor reaches its highest value when the period of the input motion is equal to the characteristic site period. More realistic site conditions produce more-complicated amplification functions, but all amplification functions are frequency-dependent. In a sense, the surficial soil layers act as a filter that amplifies certain frequencies and deamplifies others. The overall effect on site response depends on how these frequencies match up with the dominant frequencies in the input motion.

The example illustrated above is mathematically convenient, but unrealistically simple for application to actual sites. First, the assumption of rigid bedrock implies that all downward-traveling waves are perfectly reflected back up into the overlying layer. While generally quite stiff, bedrock is not perfectly rigid and therefore a portion of the energy in a downward-traveling wave is transmitted into the bedrock to continue traveling downward — as a result, the energy carried by the reflected wave that travels back up is diminished. The relative proportions of the transmitted and reflected waves depends on the ratio of the **specific impedance** of the two materials on either side of the boundary. At any rate, the amount of wave energy that remains within the surficial layer is decreased by waves radiating into the underlying rock. The resulting reduction in wave amplitudes is often referred to as **radiation damping**. Second, subsurface stratigraphy is generally more complicated than that assumed in the example. Most sites have multiple layers of different materials with different specific impedances. The boundaries between the layers may be horizontal or may be inclined, but all will reflect and refract seismic waves to produce wave fields that are much more complicated than described above. This is often particularly true in the vicinity of bridges located in fluvial geologic environments where soil stratigraphy may be the result of an episodic series of erosional and depositional events. Third, site topography is generally not flat, particularly in the vicinity of bridges which may be supported in sloping natural or man-made materials, or on man-made embankments. Topographic conditions can strongly influence the amplitude and frequency content of ground motions. Finally, subsurface conditions can be highly variable, particularly in the geologic environments in which many bridges are constructed. Conditions may be different at each end of a bridge, and even at the locations of intermediate supports — this effect is particularly true for long bridges. These factors, combined with the fact that seismic waves may reach one end of the bridge before the other, can reduce the **coherence** of ground motions. Different motions transmitted to a bridge at different support points can produce loads and displacements that would not occur in the case of perfectly coherent motions.

Evidence for Local Site Effects

Theoretical evidence for the existence of local site effects has been supplemented by instrumental and observational evidence in numerous earthquakes. Nearly 200 years ago [35], variations in damage patterns were correlated to variations in subsurface conditions; such observations have been repeated on a regular basis since that time. With the advent of modern seismographs and strong motion instruments, quantitative evidence for local site effects is now available. In the Loma Prieta earthquake, for example, strong motion instruments at Yerba Buena Island and Treasure Island were at virtually identical distances and azimuths from the hypocenter. However, the Yerba Buena Island instrument was located on a rock outcrop and the Treasure Island instrument on about 14 m of loose hydraulically placed sandy fill underlain by nearly 17 m of soft San Francisco Bay Mud. The measured motions, which differed significantly (Figure 33.14), illustrate the effects of local site effects. At a small but increasing number of locations, strong motion instruments have been placed in a boring directly below a surface instrument (Figure 33.15a). Because such vertical arrays can measure motions at the surface and at bedrock level, they allow direct computation of measured amplification functions. Such an empirical amplification function is shown in Figure 33.15b. The general similarity of the measured amplification function, particularly the strong frequency dependence, to even the simple theoretical amplification (Figure 33.13) is notable.

Methods of Analysis

Development of suitable design ground motions, and estimation of appropriate foundations loading, generally requires prediction of anticipated site response. This is usually accomplished using empirical or analytical methods. For small bridges, or for projects in which detailed subsurface information is not available, the empirical approach is more common. For larger and more important structures, a subsurface exploration program is generally undertaken to provide information for site-specific analytical prediction of site response.

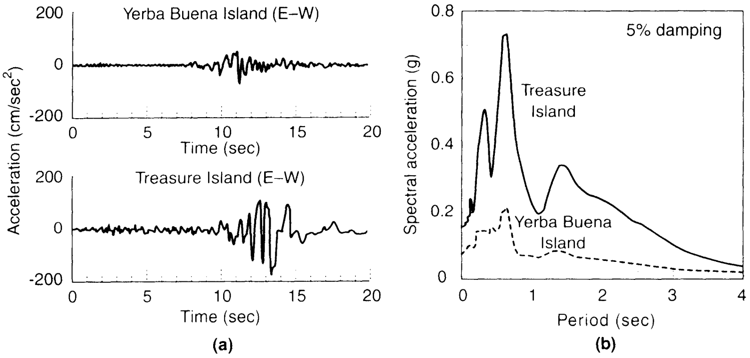

FIGURE 33.14 Ground surface motions at Yerba Buena Island and Treasure Island in the Loma Prieta earthquake. sources Kramer, S.L., *Geotechnical Earthquake Engineering*, Prentice-Hall, Upper Saddle River, NJ, 1996.)

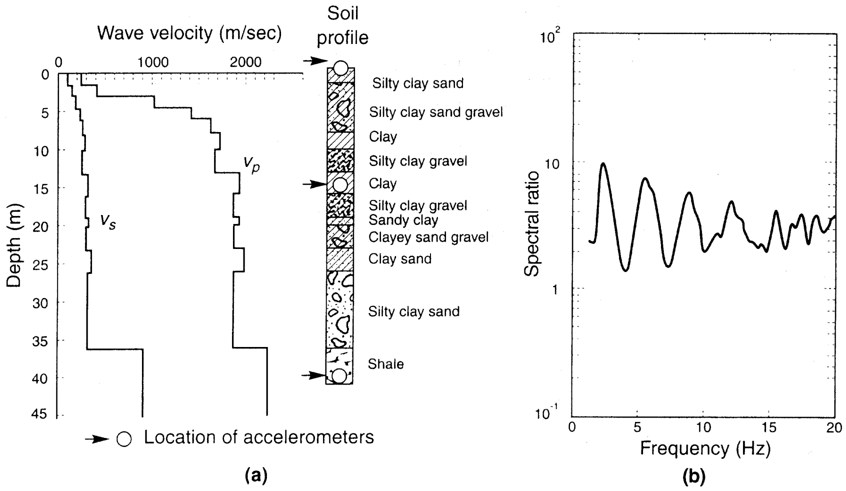

FIGURE 33.15 (a) Subsurface profile at location of Richmond Field Station downhole array, and (b) measured surface/bedrock amplification function in Briones Hills ($M_L = 4.3$) earthquake. sources Kramer, S.L., *Geotechnical Earthquake Engineering*, Prentice-Hall, Upper Saddle River, NJ, 1996.)

Empirical Methods

In the absence of site-specific information, local site effects can be estimated on the basis of empirical correlation to measured site response from past earthquakes. The database of strong ground motion records has increased tremendously over the past 30 years. Division of records within this database according to general site conditions has allowed the development of empirical correlations for different site conditions.

The earliest empirical approach involved estimation of the effects of local soil conditions on peak ground surface acceleration and spectral shape. Seed et al. [59] divided the subsurface conditions at the sites of 104 strong motion records into four categories — rock, stiff soils (<61 m), deep cohesionless soils (>76 m), and soft to medium clay and sand. Comparing average peak ground surface accelerations measured at the soil sites with those anticipated at equivalent rock sites allowed development of curves such as those shown in Figure 33.16. These curves show that soft profiles amplify peak acceleration over a wide range of rock accelerations, that even stiff soil profiles amplify peak acceleration when peak accelerations are relatively low, and that peak accelerations are deamplified at very high

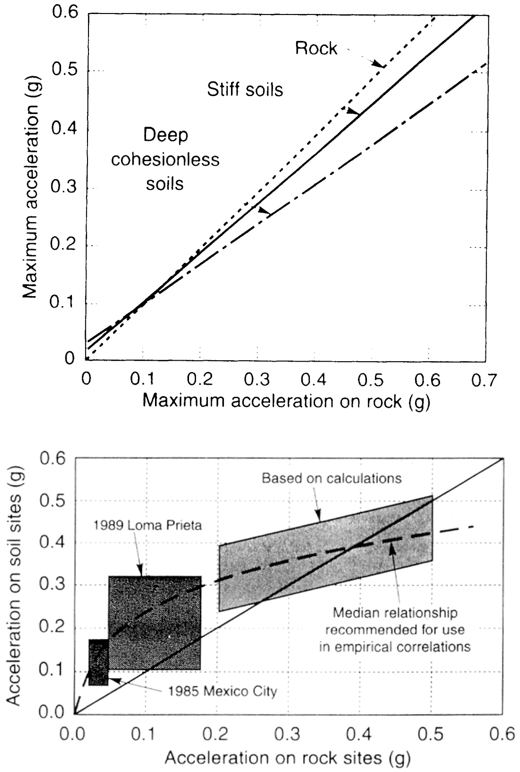

FIGURE 33.16 Approximate relationship between beak accelerations on rock and soil sites (after Seed et al. [59]; Idriss, 1990).

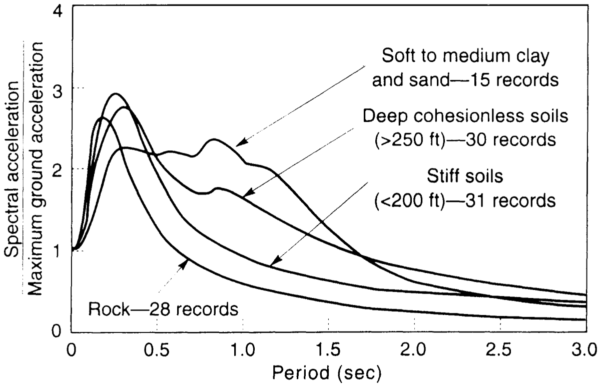

FIGURE 33.17 Average normalized response spectra (5% damping) for different local site conditions (after Seed et al. [59]).

input acceleration levels. Computation of average response spectra, when normalized by peak acceleration (Figure 33.17), showed the significant effect of local soil conditions on spectral shape, a finding that has strongly influenced the development of seismic codes and standards.

A more recent empirical approach has been to include local site conditions directly in attenuation relationships. By developing a site parameter to characterize the soil conditions at the locations of strong motion instruments and incorporating that parameter into the basic form of an attenuation

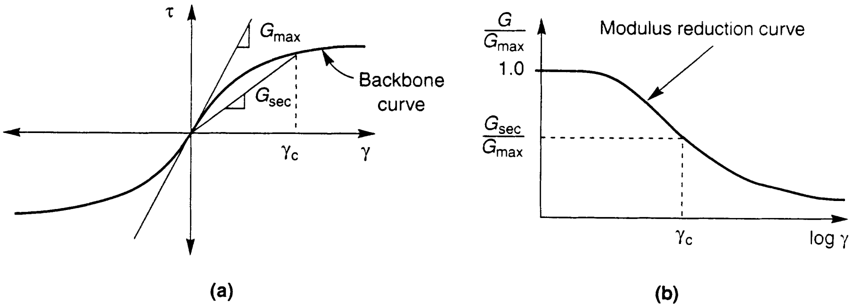

FIGURE 33.18 Relationship between backbone curve and modulus reduction curve.

relationship, regression analyses can produce attenuation relationships that include the effects of local site conditions. In such relationships, site conditions are typically grouped into different site classes on the basis of such characteristics as surficial soil/rock conditions [see the factors S_{sr} and S_{hr} in Eq. (33.13)] or average shear wave velocity within the upper 30 m of the ground surface (e.g., Boore et al. [6]). Such relationships can be used for empirical prediction of peak acceleration and response spectra, and incorporated into probabilistic seismic hazard analyses to produce uniform risk spectra for the desired class of subsurface conditions.

The reasonableness of empirically based methods for estimation of site response effects depends on the extent to which site conditions match the site conditions in the databases from which the empirical relationships were derived. It is important to recognize the empirical nature of such methods and the significant uncertainty inherent in the results they produce.

Analytical Methods

When sufficient information to characterize the geometry and dynamic properties of subsurface soil layers is available, local site effects may be computed by site-specific ground response analyses. Such analyses may be conducted in one, two, or three dimensions; one-dimensional analyses are most common, but the topography of many bridge sites may require two-dimensional analyses.

Unlike most structural materials, soils are highly nonlinear, even at very low strain levels. This nonlinearity causes soil stiffness to decrease and material damping to increase with increasing strain amplitude. The variation of stiffness with strain can be represented in two ways — by nonlinear **backbone** (stress–strain) **curves** or by **modulus reduction curves**, both of which are related as illustrated in Figure 33.18. The modulus reduction curve shows how the secant shear modulus of the soil decreases with increasing strain amplitude. To account for the effects of nonlinear soil behavior, ground response analyses are generally performed using one of two basic approaches: the **equivalent linear approach** or the **nonlinear approach**.

In the equivalent linear approach, a linear analysis is performed using shear moduli and damping ratios that are based on an initial estimate of strain amplitude. The strain level computed using these properties is then compared with the estimated strain amplitude and the properties adjusted until the computed strain levels are very close to those corresponding to the soil properties. Using this iterative approach, the effects of nonlinearity are approximated in a linear analysis by the use of *strain-compatible* soil properties. Modulus reduction and damping behavior has been shown to be influenced by soil plasticity, with highly plastic soils exhibiting higher linearity and lower damping than low-plasticity soils (Figure 33.19). The equivalent linear approach has been incorporated into such computer programs as SHAKE [53] and ProShake [18] for one-dimensional analyses, FLUSH [34] for two-dimensional analyses, and TLUSH [29] for three-dimensional analyses.

In the nonlinear approach, the equations of motion are assumed to be linear over each of a series of small time increments. This allows the response at the end of a time increment to be computed from the conditions at the beginning of the time increment and the loading applied during the time

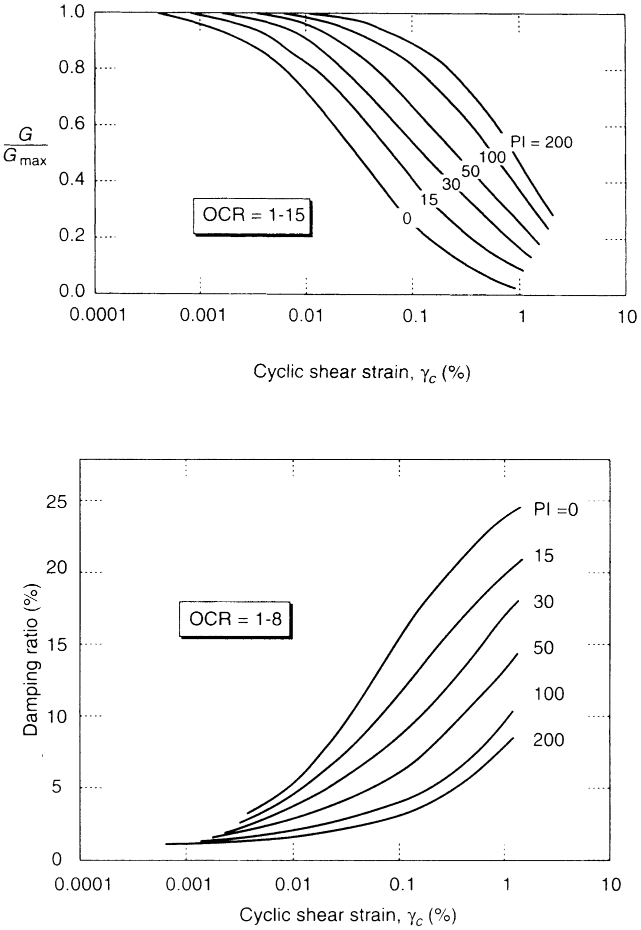

FIGURE 33.19 Equivalent linear soil behavior: (a) modulus reduction curves and (b) damping curves. (*Source*: Vucetic and Dobry, 1991.)

increment. At the end of the time increment, the properties are updated for the next time increment. In this way, the stiffness of each element of soil can be changed depending on the current and past stress conditions and hysteretic damping can be modeled directly. For seismic analysis, the nonlinear approach requires a constitutive (stress–strain) model that is capable of representing soil behavior under dynamic loading conditions. Such models can be complicated and can require calibration of a large number of soil parameters by extensive laboratory testing. With a properly calibrated constitutive model, however, nonlinear analyses can provide reasonable predictions of site response and have two significant advantages over equivalent linear analyses. First, nonlinear analyses are able to predict permanent deformations such as those associated with ground failure (Section 33.7). Second, nonlinear analyses are able to account for the generation, redistribution, and eventual dissipation of porewater pressures which makes them particularly useful for sites that may be subject to liquefaction and/or lateral spreading. The nonlinear approach has been incorporated into such computer programs as DESRA [31], TESS [48], and SUMDES for one-dimensional analysis, and TARA [21] for two-dimensional analyses. General-purpose programs such as FLAC can also be used for nonlinear two-dimensional analyses. In practice, however, the use of nonlinear analyses has lagged behind the use of equivalent linear analyses, principally because of the difficulty in characterizing nonlinear constitutive model parameters.

TABLE 33.2 Site Coefficient

Soil Type	Description	S
I	Rock of any characteristic, either shalelike or crystalline in nature (such material may be characterized by a shear wave velocity greater than 760 m/s, or by other appropriate means of classification; or Stiff soil conditions where the soil depth is less than 60 m and the soil types overlying rock are stable deposits of sands, gravels, or stiff clays.	1.0
II	Stiff clay or deep cohesionless conditions where the soil depth exceeds 60 m and the soil types overlying rock are stable deposits of sands, gravels, or stiff clays	1.2
III	Soft to medium-stiff clays and sands, characterized by 9 m or more of soft to medium-stiff clays with or without intervening layers of sand or other cohesionless soils	1.5
IV	Soft clays or silts greater than 12 m in depth; these materials may be characterized by a shear wave velocity less than 150 m/s and might include loose natural deposits or synthetic nonengineered fill	2.0

Site Effects for Different Soil Conditions

As indicated previously, soil deposits act as filters, amplifying response at some frequencies and deamplifying it at others. The greatest degree of amplification occurs at frequencies corresponding to the characteristic site period, $T_s = 4H/v_s$. Because the characteristic site period is proportional to shear wave velocity and inversely proportional to thickness, it is clear that the response of a given soil deposit will be influenced by the stiffness and thickness of the deposit. Thin and/or stiff soil deposits will amplify the short-period (high-frequency) components, and thick and/or soft soil deposits will amplify the long-period (low-frequency) components of an input motion. As a result, generalizations about site effects for different soil conditions are generally based on the average stiffness and thickness of the soil profile.

These observations of site response are reflected in bridge design codes. For example, the 1997 Interim Revision of the 1996 Standard Specifications for Highway Bridges (AASHTO, 1997) require the use of an elastic seismic response coefficient for an SDOF structure of natural period, T, taken as

$$C_s = \frac{1.2AS}{T^{2/3}} \tag{33.22}$$

where A is an acceleration coefficient that depends on the location of the bridge and S is a dimensionless site coefficient obtained from Table 33.2. In accordance with the behavior illustrated in Figure 33.17, the site coefficient prescribes increased design requirements at long periods for bridges underlain by thick deposits of soft soil (Figure 33.20).

33.7 Earthquake-Induced Settlement

Settlement is an important consideration in the design of bridge foundations. In most cases, settlement results from *consolidation*, a process that takes place relatively slowly as porewater is squeezed from the soil as it seeks equilibrium under a new set of stresses. Consolidation settlements are most significant in fine-grained soils such as silts and clays. However, the tendency of coarse-grained soils (sands and gravels) to densify due to vibration is well known; in fact, it is frequently relied upon for efficient compaction of sandy soils. Densification due to the cyclic stresses imposed by earthquake shaking can produce significant settlements during earthquakes. Whether caused by consolidation or earthquakes, bridge designers are concerned with **total settlement** and, because settlements rarely occur uniformly, also with **differential settlement**. Differential settlement can induce very large loads in bridge structures.

While bridge foundations may settle due to shearing failure in the vicinity of abutments (Chapter 30), shallow foundations (Chapter 31), and deep foundations (Chapter 32), this section

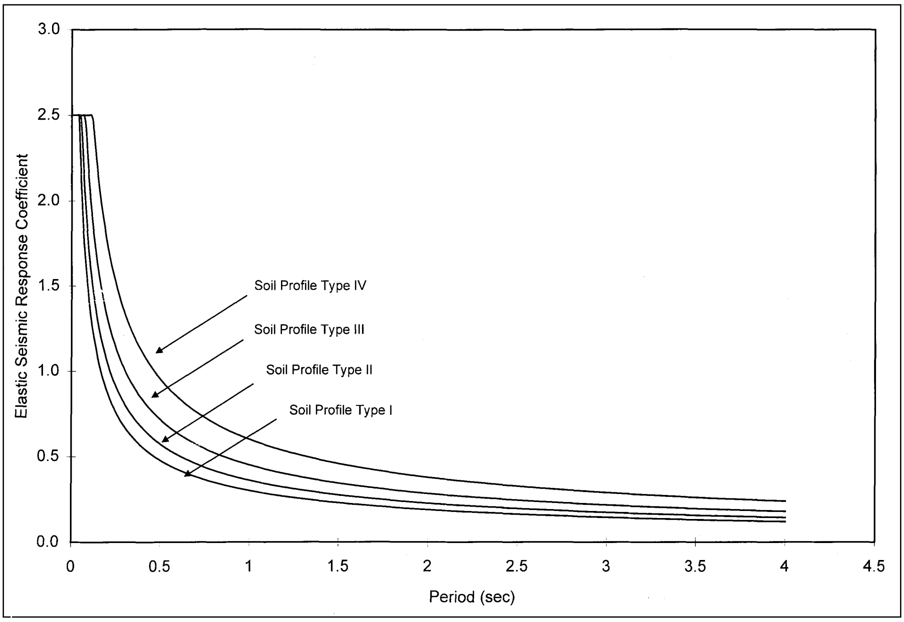

FIGURE 33.20 Variation of elastic seismic response coefficient with period for $A = 0.25$.

deals with settlement due to earthquake-induced soil densification. Densification of soils beneath shallow bridge foundations can cause settlement of the foundation. Densification of soils adjacent to deep foundations can cause downdrag loading on the foundations (and bending loading if the foundations are battered). Densification of soils beneath approach fills can lead to differential settlements at the ends of the bridge that can be so abrupt as to render the bridge useless.

Accurate prediction of earthquake-induced settlements is difficult. Errors of 25 to 50% are common in estimates of consolidation settlement, so even less accuracy should be expected in the more-complicated case of earthquake-induced settlement. Nevertheless, procedures have been developed that account for the major factors known to influence earthquake-induced settlement and that have been shown to produce reasonable agreement with many cases of observed field performance. Such procedures are generally divided into cases of dry sands and saturated sands.

Settlement of Dry Sands

Dry sandy soils are often found above the water table in the vicinity of bridges. The amount of densification experienced by dry sands depends on the density of the sand, the amplitude of cyclic shear strain induced in the sand, and on the number of cycles of shear strain applied during the earthquake. Settlements can be estimated using cyclic strain amplitudes from site response analyses with corrections for the effects of multidirectional shaking [47,58] or by simplified procedures [63]. Because of the high air permeability of sands, settlement of dry sands occurs almost instantaneously.

In the simplified procedure, the effective cyclic strain amplitude is estimated as

$$\gamma_{\text{cyc}} = 0.65 \frac{a_{\max}}{g} \frac{\sigma_v r_d}{G} \tag{33.23}$$

Because the shear modulus, G, is a function of γ_{cyc}, several iterations may be required to calculate a value of γ_{cyc} that is consistent with the shear modulus. When the low strain stiffness, $G_{\max}$ ($= \rho v_s^2$), is known, the effective cyclic strain amplitude can be estimated using Figures 33.21 and 33.22.

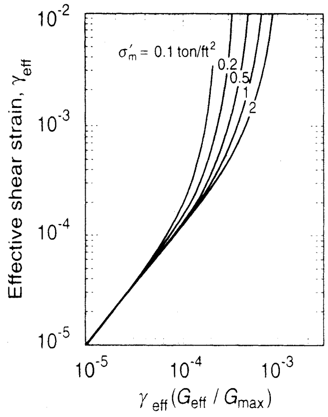

Plot for determination

FIGURE 33.21 Plot for determination of effective cyclic shear strain in sand deposits. (Tokimatsu and Seed [63]).

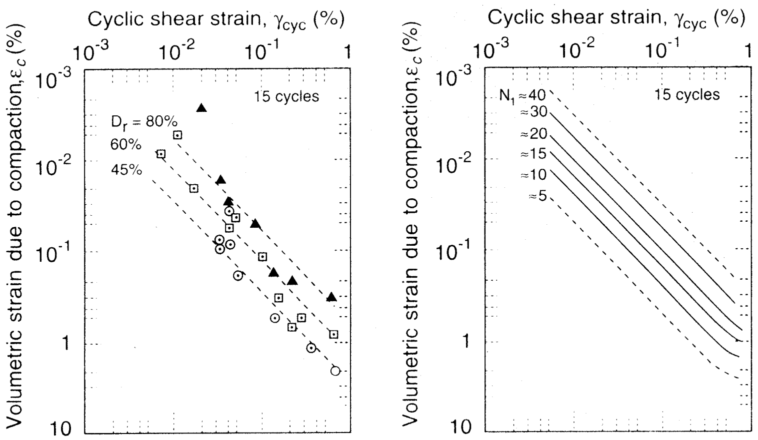

FIGURE 33.22 Relationship between volumetric strain and cyclic shear strain in dry sands as function of (a) relative density and (b) SPT resistance. (Tokimatsu and Seed [63]).

Figure 33.22 then allows the effective cyclic strain amplitude, along with the relative density or SPT resistance of the sand, to be used to estimate the volumetric strain due to densification. These volumetric strains are based on durations associated with a M = 7.5 earthquake; corrections for other magnitudes can be made with the aid of Table 33.3. The effects of multidirectional shaking are generally accounted for by doubling the computed volumetric strain. Because the stiffness, density, and cyclic shear strain amplitude generally vary with depth, a given soil deposit is usually divided into sublayers with the volumetric strain for each sublayer computed independently. The resulting settlement of each sublayer can then be computed as the product of the volumetric strain and thickness. The total settlement is obtained by summing the settlements of the individual sublayers.

Settlement of Saturated Sands

The dissipation of high excess porewater pressures generated in saturated sands (*reconsolidation*) can lead to settlement following earthquakes. Settlements of 50 to 70 cm occurred in a 5-m-thick

TABLE 33.3 Correction of Cyclic Stress Ratio for Earthquake Magnitude

Magnitude, M	5¼	6	6¾	7½	8½
$\varepsilon_{v,M}/\varepsilon_{v,M=7.5}$	0.4	0.6	0.85	1.0	1.25

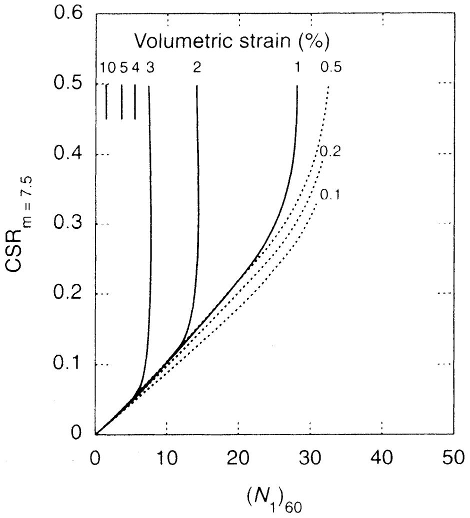

FIGURE 33.23 Plot for estimation of postliquefaction volumetric strain in saturated sands. (Tokimatsu and Seed [63]).

layer of very loose sand in the Tokachioki earthquake [44] and settlements of 50 to 100 cm were observed on Port Island and Rokko Island in Kobe, Japan following the 1995 Hyogo-ken Nambu earthquake. Because water flows much more slowly through soil than air, settlements of saturated sands occur much more slowly than earthquake-induced settlements of dry sands. Nevertheless, the main factors that influence the magnitude of saturated soil settlements are basically the same as those that influence that of dry sands.

Tokimatsu and Seed [63] developed charts to estimate the volumetric strains that develop in saturated soils. In this approach, the volumetric strain resulting from reconsolidation can be estimated from the corrected standard penetration resistance, $(N_1)_{60}$, and the cyclic stress ratio (Figure 33.23). The value of $(N_1)_{60}$ is obtained by correcting the measured standard penetration resistance, N_m, to a standard overburden pressure of 95.8 kPa (1 ton/ft^2) and to an energy of 60% of the theoretical free-fall energy of an SPT hammer using the equation:

$$(N_1)_{60} = N_m C_N \frac{E_m}{0.60\,E_{ff}} \tag{33.24}$$

where C_N is an overburden correction factor that can be estimated as $C_N = (\sigma'_{vo})^{-0.5}$, E_m is the measured hammer energy and E_{ff} is the theoretical free-fall energy. In Figure 33.23, the cyclic stress ratio, defined as $CSR_{M=7.5} = \tau_{cyc}/\sigma'_{vo}$, corresponds to a magnitude 7.5 earthquake. For other magnitudes, the corresponding value of the cyclic stress ratio can be obtained using Table 33.4. As in the case of dry sands, the soil layer is typically divided into sublayers with the total settlement taken as the sum of the products of the thickness and volumetric strain of all sublayers. In some cases, earthquake-induced porewater pressures may be insufficient to cause liquefaction but still may produce post-earthquake settlement. The volumetric strain produced by reconsolidation in such cases may be estimated from Figure 33.24.

TABLE 33.4 Correction of Cyclic Stress Ratio for Earthquake Magnitude

Magnitude, M	5¼	6	6¾	7½	8½
$CSR_M/CSR_{M=7.5}$	1.50	1.32	1.13	1.00	0.89

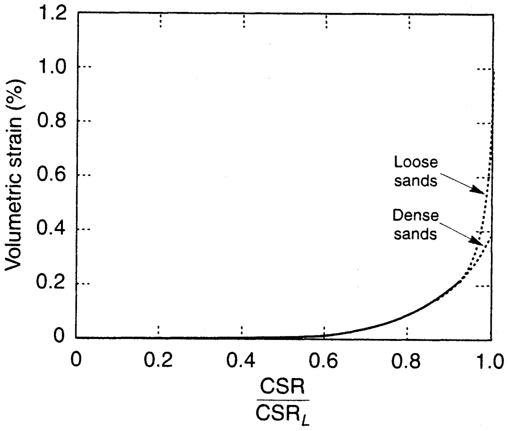

FIGURE 33.24 Plot for estimation of volumetric strain in saturated sands that do not liquefy. (Tokimatsu and Seed [63]).

33.8 Ground Failure

Strong earthquake shaking can produce a dynamic response of soils that is so energetic that the stress waves exceed the strength of the soil. In such cases, ground failure characterized by permanent soil deformations may occur. Ground failure may be caused by weakening of the soil or by temporary exceedance of the strength of the soil by transient inertial stresses. The former case results in phenomena such as liquefaction and lateral spreading; the latter in inertial failures of slopes and retaining wall backfills.

Liquefaction

The term *liquefaction* has been widely used to describe a range of phenomena in which the strength and stiffness of a soil deposit are reduced due to the generation of porewater pressure. It occurs most commonly in loose, saturated sands, although it has also been observed in gravels and non-plastic silts. The effects of liquefaction can range from massive landslides with displacements measured in tens of meters to relatively small slumps or spreads with small displacements. Many bridges, particularly those that cross bodies of water, are located in areas with geologic and hydrologic conditions that tend to produce liquefaction.

The mechanisms that produce liquefaction-related phenomena can be divided into two categories. The first, **flow liquefaction**, can occur when the shear stresses required for static equilibrium of a soil mass is greater than the shear strength of the soil in its liquefied state. While not common, flow liquefaction can produce tremendous instabilities known as **flow failures**. In such cases, the earthquake serves to trigger liquefaction, but the large deformations that result are actually driven by the preexisting static stresses. The second phenomenon, **cyclic mobility**, occurs when the initial static stresses are less than the strength of the liquefied soil. The effects of cyclic mobility lead to deformations that develop incrementally during the period of earthquake shaking, and are commonly called **lateral spreading**.

Lateral spreading can occur on very gentle slopes, in the vicinity of free surfaces such as riverbanks, and beneath and adjacent to embankments. Lateral spreading occurs much more frequently than flow failure, and can cause significant distress to bridges and their foundations.

Liquefaction Susceptibility

The first step in an evaluation of liquefaction hazards is the determination of whether or not the soil is susceptible to liquefaction. If the soils at a particular site are not susceptible to liquefaction, liquefaction hazards do not exist and the liquefaction hazard evaluation can be terminated. If the soil is susceptible, however, the issues of initiation and effects of liquefaction must be considered.

Liquefaction occurs most readily in loose, clean, uniformly graded, saturated soils. Therefore, geologic processes that sort soils into uniform grain size distributions and deposit them in loose states produce soil deposits with high liquefaction susceptibility. As a result, fluvial deposits, and colluvial and aeolian deposits when saturated, are likely to be susceptible to liquefaction. Liquefaction also occurs in alluvial, beach, and estuarine deposits, but not as frequently as in those previously listed. Because bridges are commonly constructed in such geologic environments, liquefaction is a frequent and important consideration in their design.

Liquefaction susceptibility also depends on the stress and density characteristics of the soil. Very dense soils, even if they have the other characteristics listed in the previous paragraph, will not generate high porewater pressures during earthquake shaking and hence are not susceptible to liquefaction. The minimum density at which soils are not susceptible to liquefaction increases with increasing effective confining pressure. This characteristic indicates that, for a soil deposit of constant density, the deeper soils are more susceptible to liquefaction than the shallower soils. For the general range of soil conditions encountered in the field, cohesionless soils with $(N_1)_{60}$ values greater than 30 or normalized cone penetration test (CPT) tip resistances (q_{c1N}, see next section) greater than about 175 are generally not susceptible to liquefaction.

Initiation of Liquefaction

The fact that a soil deposit is susceptible to liquefaction does not mean that liquefaction will occur in a given earthquake. Liquefaction must be triggered by some disturbance, such as earthquake shaking with sufficient strength to exceed the liquefaction resistance of the soil. Even a liquefaction-susceptible soil will have some liquefaction resistance. Evaluating the potential for the occurrence of liquefaction (liquefaction potential) involves comparison of the loading imposed by the anticipated earthquake with the liquefaction resistance of the soil. Liquefaction potential is most commonly evaluated using the cyclic stress approach in which both earthquake loading and liquefaction resistance are expressed in terms of cyclic stresses, thereby allowing direct and consistent comparison.

Characterization of Earthquake Loading

The level of porewater pressure generated by an earthquake is related to the amplitude and duration of earthquake-induced shear stresses. Such shear stresses can be predicted in a site response analysis using either the equivalent linear method or nonlinear methods. Alternatively, they can be estimated using a simplified approach that does not require site response analyses.

Early methods of liquefaction evaluation were based on the results of cyclic triaxial tests performed with harmonic (constant-amplitude) loading, and it remains customary to characterize loading in terms of an equivalent shear stress amplitude,

$$\tau_{\mathrm{cyc}} = 0.65\tau_{\mathrm{max}} \tag{33.25}$$

When sufficient information is available to perform site response analyses, it is advisable to compute τ_{max} in a site response analysis and use Eq. (33.6) to compute τ_{cyc}. When such information is not available, τ_{cyc} at a particular depth can be estimated as

$$\tau_{\mathrm{cyc}} = 0.65 \frac{a_{\max}}{g} \sigma_v r_d \tag{33.26}$$

where $a_{\max}$ is the peak ground surface acceleration, g is the acceleration of gravity, σ_v is the total vertical stress at the depth of interest, and r_d is the value of a site response reduction factor which can be estimated from

$$r_d = \frac{1.0 - 0.4113z^{0.5} + 0.04052z + 0.001753z^{1.5}}{1.0 - 0.4177z^{0.5} + 0.05729z - 0.006205z^{1.5} + 0.001210z^2} \tag{33.27}$$

where z is the depth of interest in meters. For evaluation of liquefaction potential, it is common to normalize τ_{cyc} by the initial (pre-earthquake) vertical effective stress, thereby producing the **cyclic stress ratio** (CSR)

$$\mathrm{CSR} = \frac{\tau_{\mathrm{cvc}}}{\sigma'_{vo}} \tag{33.28}$$

Characterization of Liquefaction Resistance

While early liquefaction potential evaluations relied on laboratory tests to measure liquefaction resistance, increasing recognition of the deleterious effects of sampling disturbance on laboratory test results has led to the use of field tests for measurement of liquefaction resistance. Although the use of new soil freezing and sampling techniques offers considerable promise for acquisition of undisturbed samples, liquefaction resistance is currently evaluated using *in situ* tests such as the standard penetration test (SPT) and the CPT *and* observations of liquefaction behavior in past earthquakes.

Case histories in which liquefaction was and was not observed can be analyzed to obtain empirical estimates of liquefaction resistance. By characterizing each of a series of case histories in terms of a loading parameter, $\mathcal{L}$, and a resistance parameter, $\mathcal{R}$, all combinations of $\mathcal{L}$ and $\mathcal{R}$ can be plotted with symbols that indicate whether liquefaction was observed or was not observed (Figure 33.25).

In this approach, the cyclic stress ratio induced in the soil for each case history is used as the loading parameter and an *in situ* test measurement is used as the resistance parameter. Two *in situ* tests are commonly used — the SPT which produces the resistance parameter $(\mathrm{N}_1)_{60}$, and the CPT which produces the resistance parameter, $q_{c1\mathrm{N}}$. Because the value of the cyclic stress ratio given by the curve represents the minimum cyclic stress ratio required to produce liquefaction, it is commonly referred to as the **cyclic resistance ratio**, CRR.

Because liquefaction involves the cumulative buildup of porewater pressure, the ultimate porewater pressure level is a function of the duration of ground shaking. In the development of procedures for evaluation of liquefaction potential, duration was implicitly correlated to earthquake magnitude. As a result, the procedures have been keyed to magnitude 7.5 earthquakes with corrections developed that can be applied for other magnitudes. The procedures have also been keyed to clean sands (<5% fines), again with corrections developed for application to silty sands.

Recent review of SPT-based procedures for characterization of CRR resulted in recommendation of the curve shown in Figure 33.26. This CRR curve is for clean sand and magnitude 7.5 earthquakes. For a silty sand with fines content, FC, an equivalent clean sand SPT resistance can be computed from

$$(N_1)_{60\text{-cs}} = \alpha + \beta\ (N_1)_{60} \tag{33.29}$$

where

$\alpha = 0$ and $\beta = 1.0$ for $\mathrm{FC} < 5\%$

$\alpha = \exp[1.76 - 190/\mathrm{FC}^2]$ and $\beta = 0.99 + FC^{1.5}/1000$ for $5\% < \mathrm{FC} < 35\%$

$\alpha = 5.0$ and $\beta = 1.2$ for $\mathrm{FC} > 35\%$

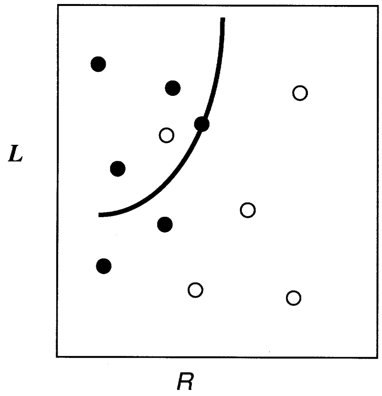

FIGURE 33.25 Discrimination between case histories in which liquefaction was observed (solid circles) and was not observed (open circles). Curve represents conservative estimate of resistance, $\mathcal{R}$, for given level of loading, $\mathcal{L}$.

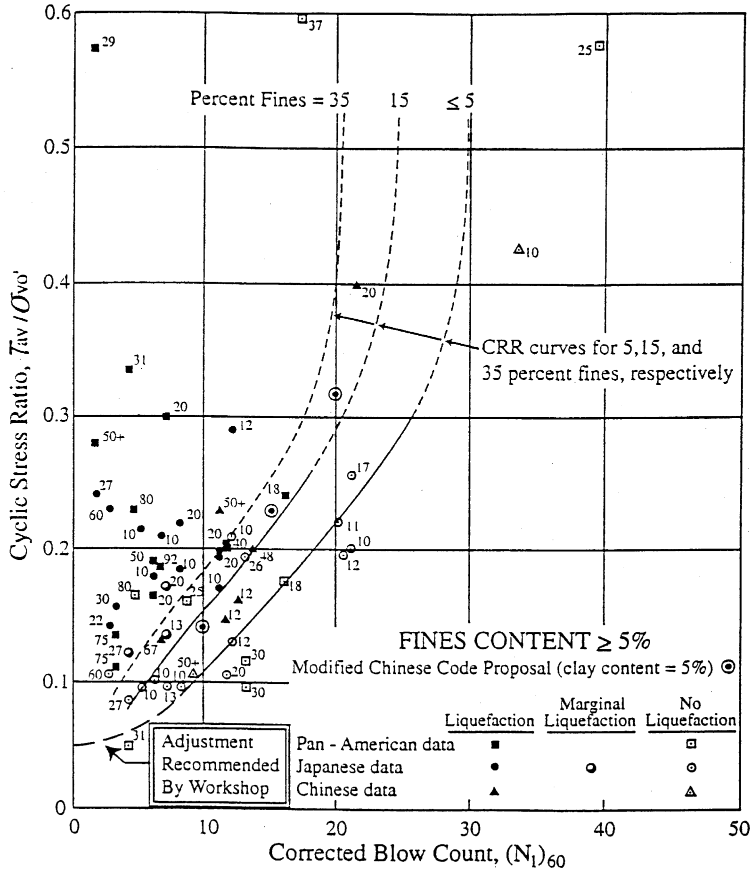

FIGURE 33.26 Relationship between cyclic stress ratios causing liquefaction and $(N_1)_{60}$ values for clean sand (after Youd and Idriss, 1998).

TABLE 33.5 Magnitude Scaling Factor

Magnitude, M	MSF
5.5	2.20–2.80
6.0	1.76–2.10
6.5	1.44–1.60
7.0	1.19–1.25
7.5	1.00
8.0	0.84
8.5	0.72

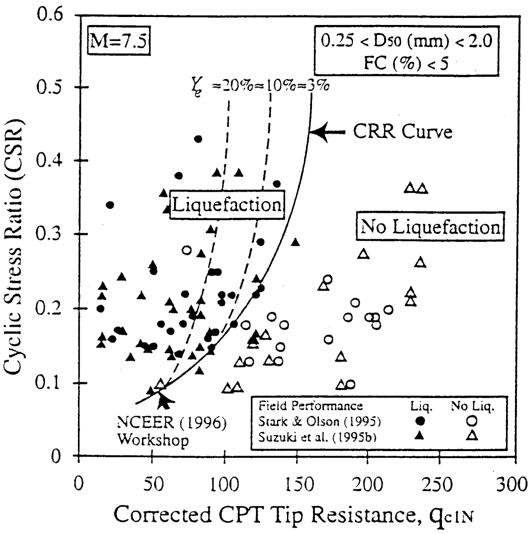

FIGURE 33.27 Relationship between cyclic stress ratios causing liquefaction and $(q_c)_1$ values for clean sand (after Youd and Idriss, 1998).

Correction for magnitudes other than 7.5 is accomplished by correcting the CRR according to

$$\mathrm{CRR}_M = \mathrm{CRR}_{7.5} \times \mathrm{MSF} \tag{33.30}$$

where MSF is a magnitude scaling factor obtained from Table 33.5.

The CPT offers two distinct advantages over the SPT for evaluation of liquefaction resistance. First, the CPT provides a nearly continuous profile of penetration resistance, a characteristic that allows it to identify thin layers that can easily be missed in an SPT-based investigation. Second, the CPT shows greater consistency and repeatability than the SPT. However, the CPT is a more recent development and there is less professional experience with it than with the SPT, particularly in the United States. As more data correlating CPT resistance to liquefaction resistance become available, the CPT is likely to be come the primary *in situ* test for evaluation of liquefaction potential. At present, however, a general consensus on the most appropriate technique for CPT-based evaluation of liquefaction potential has not emerged. One of the most well-developed procedures for CPT-based evaluation of liquefaction potential was described by Robertson and Wride. In this procedure, the measured CPT resistance, q_c, is normalized to a dimensionless resistance

$$q_{c1N} = C_Q \frac{q_c}{p_a} \tag{33.31}$$

where $C_Q = \left(p_a/\sigma'_{vo}\right)^n$, p_a is atmospheric pressure, and n is an exponent that ranges from 0.5 (clean sand) to 1.0 (clay). A maximum C_Q value of 2.0 is generally applied to CPT data at shallow depths. Soil type can be inferred from CPT tip resistance, q_c, and sleeve resistance, f_s, with the aid of a soil behavior type index

$$I_c = \sqrt{(3.47 - \log Q)^2 + (1.22 + \log F)^2} \tag{33.32}$$

where

$$Q = C_Q \frac{q_c - \sigma_{vo}}{p_a}$$

$$F = \frac{f_s}{q_c - \sigma_{vo}} \times 100\%$$

If I_c (computed with $n = 1.0$) is greater than 2.6, the soil is considered too clayey to liquefy. If I_c (computed with $n = 0.5$ and $Q = q_{c1N}$) is less than 2.6, the soil is most likely granular and nonplastic and capable of liquefying. If I_c (computed with $n = 0.5$ and $Q = q_{c1N}$) is greater than 2.6, however, the soil is likely to be very silty and possibly plastic; in this case, I_c should be recalculated with $n = 0.7$ and $Q = q_{c1N}$. Once I_c has been determined, the effects of fines and plasticity can be considered by computing the clean sand normalized tip resistance

$$q_{c1N\text{-cs}} = K_c\, q_{c1N} \tag{33.33}$$

where

$K_c = 1.0$ for $I_c < 1.64$

$K_c = -0.403 I_c^4 + 5.581 I_c^3 - 21.63 I_c^2 + 33.75 I_c - 17.88$ for $I_c > 1.64$

With the clean sand normalized tip resistance, $\text{CRR}_{7.5}$ can be determined using Figure 33.27. For other magnitudes, the appropriate value of CRR can be obtained using the same magnitude scaling factor used for the SPT-based procedure, (Eq. 30). Other procedures for CPT-based evaluation of liquefaction potential include those of Seed and De Alba (57), Mitchell and Tseng [39], and Olson [46].

Liquefaction resistance has also been correlated to other *in situ* test measurements such as shear wave velocity [62,64], dilatometer index, and Becker penetration tests. In addition, probabilistic approaches that yield a probability of liquefaction have also been developed [32].

Lateral Spreading

Lateral spreading has often caused damage to bridges and bridge foundations in earthquakes. Lateral spreading generally involves the lateral movement of soil at and below the ground surface, often in the form of relatively intact surficial blocks riding on a mass of softened and weakened soil. The lateral soil movement can impose large lateral loads on abutments and wingwalls, and can induce large bending moments in pile foundations. The damage produced by lateral spreading is closely related to the magnitude of the lateral soil displacements.

Because cyclic mobility, the fundamental phenomenon that produces lateral spreading, is so complex, analytical procedures for prediction of lateral spreading displacements have not yet reached the point at which they can be used for design. As a result, currently accepted procedures for prediction of lateral spreading displacements are empirically based.

Bartlett and Youd [1] used multiple regression on a large database of lateral spreading case histories to develop empirical expressions for lateral spreading ground surface displacements. Two expressions were developed — a ground slope expression for sites with gentle, uniformly sloping

TABLE 33.6 Range of Verified Values for Eq. 33.32

Input Parameter	Range of Values
Magnitude	$6.0 < M_w < 8.0$
Free-face ratio	$1.0\% < W < 20\%$
Thickness of loose layer	$0.3 \text{ m} < T_{15} < 12 \text{ m}$
Fines content	$0\% < F_{15} < 50\%$
Mean grain size	$0.1 \text{ mm} < (D_{50})_{15} < 1.0 \text{ mm}$
Ground slope	$0.1\% < S < 6\%$
Depth to bottom of section	Depth to bottom of liquefied zone <15 m

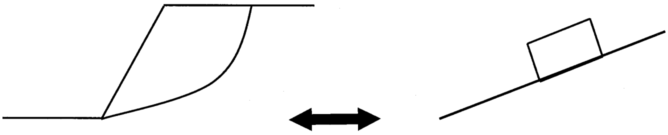

FIGURE 33.28 Illustration of sliding block analogy for evaluation of permanent slope displacements.

surfaces, and a free-face expression for sites near steep banks. For the former, displacements can be estimated from

$$\begin{aligned}\log D_H = &-16.3658 + 1.1782 M_w - 0.9275 \log R - 0.0133R + 0.4293 \log S \\ &+ 0.3483 \log T_{15} + 4.5720 \log(100 - F_{15}) - 0.9224 \left(D_{50}\right)_{15}\end{aligned} \tag{33.34a}$$

where D_H is the estimated lateral ground displacement in meters, M_w is the moment magnitude, R is the horizontal distance from the seismic energy source in km, S is the ground slope in percent, T_{15} is the cumulative thickness of saturated granular layers with $(N_1)_{60} < 15$ in meters, F_{15} is the average fines content for the granular layers comprising T_{15} in percent, and $(D_{50})_{15}$ is the average mean grain size for the granular layers comprising T_{15} in millimeters. For free-face sites, displacements can be estimated from

$$\begin{aligned}\log D_H = &-16.3658 + 1.1782 M_w - 0.9275 \log R - 0.0133R + 0.6572 \log W \\ &+ 0.3483 \log T_{15} + 4.5720 \log(100 - F_{15}) - 0.9224 \left(D_{50}\right)_{15}\end{aligned} \tag{33.34b}$$

where W is the ratio of the height of the bank to the horizontal distance between the toe of the bank and the point of interest. With these equations, 90% of the predicted displacements were within a factor of two of those observed in the corresponding case histories. The range of parameters for which the predicted results have been verified by case histories is presented in Table 33.6.

Global Instability

Ground failure may also occur due to the temporary exceedance of the shear strength of the soil by earthquake-induced shear stresses. These failures may take the form of large, deep-seated soil failures that can encompass an entire bridge abutment or foundation as illustrated in Figure 33.28. The potential for such failures, often referred to as global instabilities, must be evaluated during design.

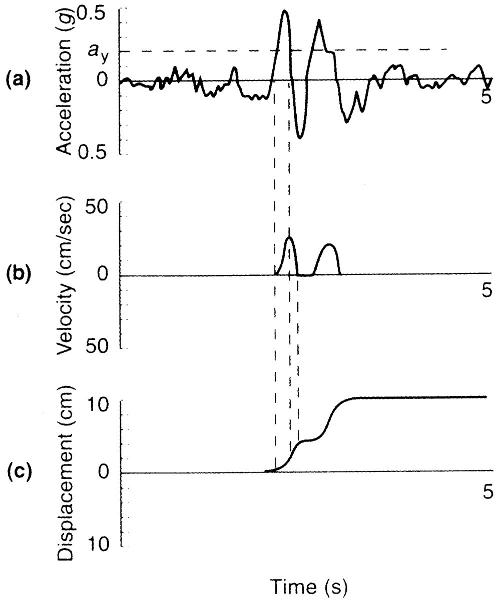

FIGURE 33.29 Illustration of computation of permanent slope displacements using sliding block method.

Historically, inertial failures were evaluated using **pseudo-static methods** in which the transient, dynamic effects of earthquake shaking were represented by constant, pseudo-static accelerations. The resulting destabilizing pseudo-static forces were included in a limit equilibrium analysis to compute a pseudo-static factor of safety. A pseudo-static factor of safety greater than one was considered indicative of stability. However, difficulty in selection of the pseudo-static acceleration, interpretation of the significance of computed factors of safety less than 1, and increasing recognition that serviceability is closely related to permanent deformations led to the development of alternative approaches.

The most common current procedure uses pseudo-static principles to establish the point at which permanent displacements would begin, but then uses a simple slope analogy to estimate the magnitude of the resulting permanent displacements. This procedure is commonly known as the sliding block procedure [43]. By using the common assumptions of rigid, perfectly plastic behavior embedded in limit equilibrium analyses, a potentially unstable slope is considered to be analogous to a block resting on an inclined plane (Figure 33.28) in the sliding block procedure. In both cases, base accelerations above a certain level will result in permanent relative displacements of the potentially unstable mass.

In the sliding block procedure, a pseudo-static analysis is performed to determine the horizontal pseudo-static acceleration that produces a factor of safety of 1.0. This pseudo-static acceleration, referred to as the **yield acceleration**, represents the level of acceleration above which permanent slope displacements are expected to occur. When the input acceleration exceeds the yield acceleration, the shear stress between the sliding block and the plane exceeds the available shear resistance and the block is unable to accelerate as quickly as the underlying plane. As a result, there is a relative acceleration between the block and the plane that lasts until the shear stress drops below the strength long enough to decelerate the block to zero relative acceleration. Integration of the relative acceleration over time yields a relative velocity, and integration of the relative velocity produces the relative displacement between the block and the plane. By this process, illustrated in Figure 33.29, the sliding block procedure allows estimation of the permanent displacement of a slope.

For embankments subjected to ground motions perpendicular to their axes, Makdisi and Seed [36] developed a simplified procedure for estimation of earthquake-induced displacements based

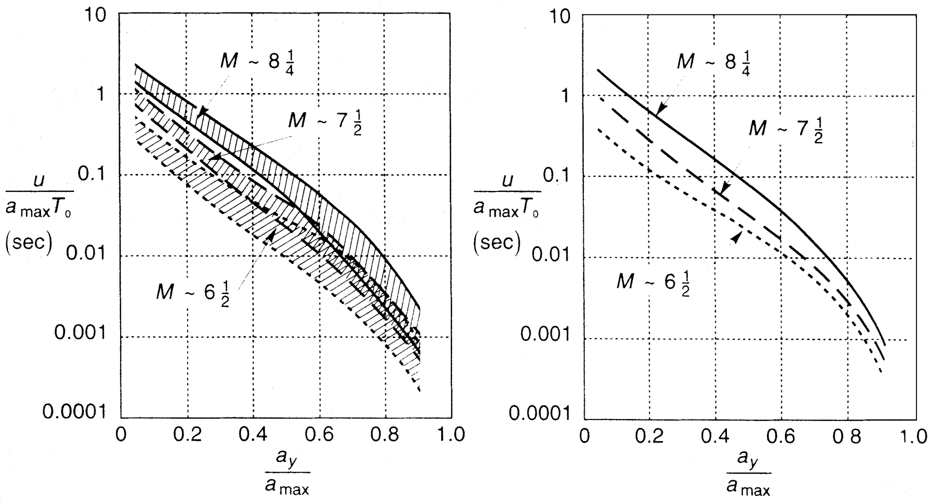

FIGURE 33.30 Variation of normalized permanent slope displacement with yield acceleration for earthquakes of different magnitudes: (a) summary for several different earthquakes and embankments and (b) average values (after Makdisi and Seed [36]).

on sliding block analyses of dams and embankments subjected to several recorded and synthetic input motions. By knowing the yield acceleration of the slope in addition to the peak acceleration and fundamental period of the embankment, Figure 33.30 can be used to estimate permanent slope displacements.

Retaining Structures

Earth-retaining structures are commonly constructed as parts of bridge construction projects and, in the form of abutment walls and wingwalls, as parts of bridge structures themselves. However, there are many different types of retaining structures, several of which have been developed in recent years. Historically, rigid retaining structures have been most commonly used; their static design is based on classical earth pressure theories. However, newer types of retaining structures, such as flexible anchored walls, soil nailed walls, and reinforced walls, have required the development of new approaches, even for static conditions. Under seismic conditions, classical earth pressure theories can be extended in a logical way to account for the effects of earthquake shaking, but seismic design procedures for the newer types of retaining structures remain under development.

Free-standing rigid retaining structures typically maintain equilibrium through the development of active and passive earth pressures that develop as the wall translates and rotates under the action of the imposed stresses. By assuming that static stresses develop through mobilization of the shear strength of the backfill soil on a planar potential failure surface, Coulomb earth pressure theory predicts a static active thrust of

$$P_A = \frac{1}{2} K_A \gamma H^2 \tag{33.35}$$

where

$$K_A = \frac{\cos^2(\phi - \theta)}{\cos^2\theta \cos(\delta + \theta)\left[\dfrac{\sin(\delta + \phi)\sin(\phi - \beta)}{\cos(\delta + \theta)\cos(\beta - \theta)}\right]^2}$$

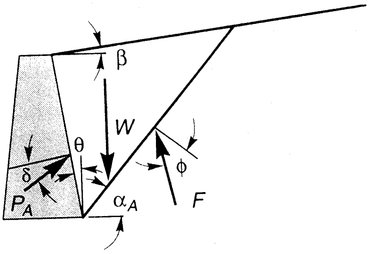

FIGURE 33.31 Illustration of variables for computation of active Earth thrust.

δ is the angle of interface friction between the wall and the soil, and β and θ are as shown in Figure 33.31.

Under earthquake shaking, active earth pressures tend to increase above static levels. In one of the first geotechnical earthquake engineering analyses, Okabe [45] and Mononobe and Matsuo [40] developed a pseudo-static extension of Coulomb theory to predict the active earth thrust under seismic conditions. Assuming pseudo-static accelerations of $a_h = k_h g$ and $a_v = k_v g$ in the horizontal and vertical directions, respectively, the Mononobe–Okabe total thrust is given by

$$P_{AE} = \frac{1}{2} K_{AE} \gamma H^2 (1 - k_v) \tag{33.36}$$

where

$$K_{AE} = \frac{\cos^2(\phi - \theta - \psi)}{\cos\psi \cos^2\theta \cos(\delta + \theta + \psi)\left[1 + \sqrt{\dfrac{\sin(\delta + \phi)\sin(\phi - \beta - \psi)}{\cos(\delta + \theta + \psi)\cos(\beta - \theta)}}\right]^2}$$

where $\phi - \beta \ge \psi$ and $\Psi = \tan^{-1}[k_h/(1 - k_v)]$. Although the assumptions used in the Mononobe-Okabe analysis imply that the total active thrust should act at a height of $H/3$ above the base of the wall, experimental results indicate that it acts at a higher point. The total active thrust of Eq. (33.36) can be divided into a static component, P_A, given by Eq. (33.35), and a dynamic component,

$$\Delta P_{AE} = P_{AE} - P_A \tag{33.37}$$

which acts at a height of approximately $0.6H$ above the base of the wall. On this basis, the total active thrust can be taken to act at a height

$$h = \frac{P_A H/3 + \Delta P_{AE}(0.6H)}{P_{AE}} \tag{33.38}$$

above the base of the wall.

When retaining walls are braced against lateral movement at top and bottom, as can occur with abutment walls, the shear strength of the soil will not be fully mobilized under static or seismic conditions. As a result, the limiting conditions of minimum active or maximum passive conditions cannot be developed. In such cases, it is common to estimate lateral Earth pressures using the elastic solution of Wood [69] for a linear elastic material of height, H, trapped between rigid walls separated by a horizontal distance, L. For motions at less than half the fundamental frequency of the unrestrained

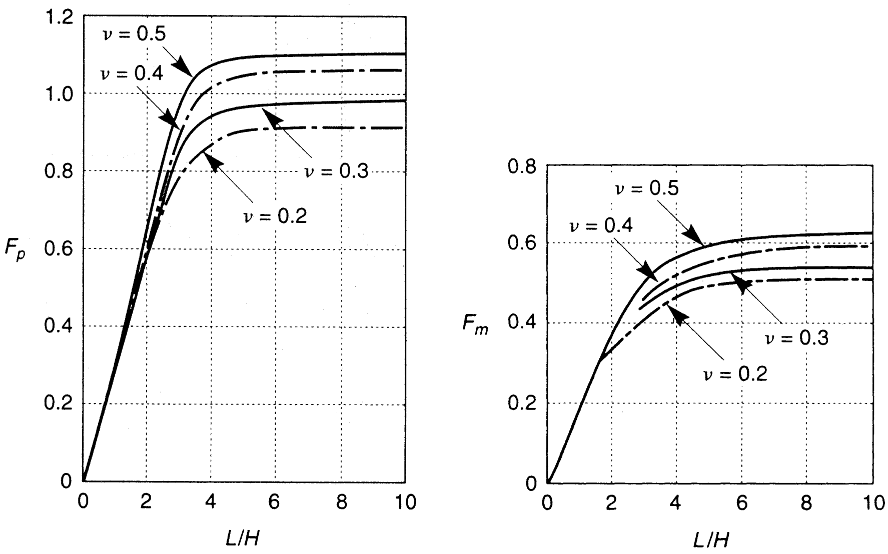

(a)

(b)

FIGURE 33.32 Charts for determination of (a) dimensionless thrust factor and (b) dimensionless moment factor for various geometries and Poisson ratios (after Wood [69]).

backfill ($f_o = v_s/4H$) the dynamic thrust and dynamic overturning moment (about the base of the wall) can be expressed as

$$\Delta P_{eq} = \gamma\, H^2 \frac{a_h}{g} F_p \tag{33.39}$$

$$\Delta M_{eq} = \gamma\, H^3 \frac{a_h}{g} F_m \tag{33.40}$$

where a_h is the amplitude of the harmonic base acceleration and F_p and F_m are dimensionless factors that can be obtained from Figure 33.32. It should be noted that Eqs. 33.39 and 33.40 refer to dynamic thrusts and moments; static thrusts and moments must be added to obtain total thrusts and moments.

33.9 Soil Improvement

When existing subsurface conditions introduce significant seismic hazards that adversely affect safety or impact construction costs, improved performance may be achieved through a program of soil improvement. A variety of techniques are available for soil improvement and may be divided into four main categories: densification, drainage, reinforcement, and grouting/mixing. Each soil improvement technique has advantages and disadvantages that influence the cost and effectiveness under different circumstances. Soil improvement techniques for both seismic and nonseismic areas are described in detail in such references as Welsh [67], Van Impe [65], Hausmann [27], Broms [8], Bell [2], and Mosely [41].

Densification Techniques

Virtually all mechanical properties of soil (e.g., strength, stiffness, etc.) improve with increasing soil density. This is particularly true when earthquake problems are considered — the tendency of loose soils to densify under dynamic loading is responsible for such hazards as liquefaction, lateral spreading, and earthquake-induced settlement. This tendency can be used to advantage, however, as most densification techniques rely on vibrations to densify granular soil efficiently. Because fines inhibit densification for much the same reason as they inhibit liquefaction, densification techniques are most efficient in clean sands and gravels.

Vibratory densification of large volumes of soil can be accomplished most economically by dynamic compaction. In this procedure, a site is densified by repeatedly lifting and dropping a heavy weight in a grid pattern across the surface of the site. By using weights that can range from 53 to 267 kN and drop heights of 10 to 30 m, densification can be achieved to depths of up to 12 m. The process is rather intrusive in terms of ground surface disturbance, noise, dust, and vibration of surrounding areas, so it is used primarily in undeveloped areas. Vibrations from probes that penetrate below the ground surface have also proved to be effective for densification. Vibroflotation, for example, is accomplished by lowering a vibrating probe into the ground (with the aid of water jets, in some cases). By vibrating the probe as it is pulled back toward the surface, a column of densified soil surrounding the vibroflot is produced. Gravel or crushed stone may be introduced into the soil at the surface or, using a bottom-feed vibroflot, at the tip of the probe to form stone columns. Blasting can also be used to densify cohesionless soils. Blast densification is usually accomplished by detonating multiple explosive charges spaced vertically at distances of 3 to 6 m in borings spaced horizontally at distances of 5 to 15 m. The charges at different elevations are often detonated at small time delays to enhance the amplitude, and therefore the densification capacity, of the blast waves. Two or three rounds of blasting, with later rounds detonated at locations between those of the earlier rounds, are often used to achieve the desired degree of densification. Finally, densification may be achieved using static means using compaction grouting. Compaction grouting involved the injection of very low slump (usually less than 25 mm) cementitious grout into the soil under high pressure. The grout forms an intact bulb or column that densifies the surrounding soil by displacement. Compaction grouting may be performed at a series of points in a grid or along a line. Grout points are typically spaced at distances of about 1 to 4 m, and have extended to depths of 30 m.

Drainage Techniques

Excessive soil and foundation movements can often be eliminated by lowering the groundwater table, and construction techniques for dewatering are well developed. The buildup of high porewater pressures in liquefiable soils can also be suppressed using drainage techniques, although drainage alone is rarely relied upon for mitigation of liquefaction hazards. Stone columns provide means for rapid drainage by horizontal flow, but also improve the soil by densification (during installation) and reinforcement.

Reinforcement Techniques

The strength and stiffness of some soil deposits can be improved by installing discrete inclusions that reinforce the soil. Stone columns are columns of dense angular gravel or crushed stone (stone columns) that reinforce the soil in which they are installed. Stone columns also improve the soil due to their drainage capabilities and the densification and lateral stress increase that generally occurs during their installation. Granular soils can also be improved by the installation of compaction piles, usually prestressed concrete or timber, driven in a grid pattern and left in place. Compaction piles can often increase relative densities to 75 to 80% within a distance of 7 to 12 pile diameters. Drilled inclusions such as drilled shafts or drilled piers have been used to stabilize many slopes, although the difficulty in drilling through loose granular soils limits their usefulness for slopes with liquefiable soils. Soil nails, tiebacks, micropiles, and root piles have also been used.

Grouting/Mixing Techniques

The characteristics of many soils can be improved by the addition of cementitious materials. Introduced by injection or mixing, these materials both strengthen the contacts between soil grains and fill the space between the grains. Grouting involves injection of cementitious materials into the voids of the soil or into fractures in the soil; in both cases, the particle structure of the majority of the soil remains intact. In mixing, the cementitious materials are mechanically or hydraulically mixed into the soil, completely destroying the initial particle structure.

Permeation grouting involves the injection of low-viscosity grouts into the voids of the soil without disturbing the particle structure. Both particulate grouts (aqueous suspensions of cement, fly ash, bentonite, microfine cement, etc.) and chemical grouts (silica and lignin gels, or phenolic and acrylic resins) may be used. The more viscous particulate grouts are generally used in coarser-grained soils with large voids such as gravels and coarse sands; chemical grouts can be used in fine sands. The presence of fines can significantly reduce the effectiveness of permeation grouting. Grout pipes are usually arranged in a grid pattern at spacings of 1.2 to 2.4 m and can produce grouted soil strengths of 350 to 2100 kPa. Intrusion grouting involves the injection of more viscous (and hence stronger) cementitious grouts under pressure to cause controlled fracturing of the ground. The first fractures generally follow weak bedding planes or minor principal stress planes; after allowing the initially placed grout to cure, repeated grouting fractures the soil along additional planes, eventually producing a three-dimensional network of intersecting grout lenses.

Using a mechanical system consisting of hollow stem augers and rotating paddles, soil mixing produces an amorphous mixture of soil and cementitious material. The soil-mixing process produces columns of soil–cement that can be arranged in a grid pattern or in a linear series of overlapping columns to produce subsurface walls and/or cellular structures. Soil mixing, which can be used in virtually all inorganic soils, has produced strengths of 1400 kPa and improvement to depths of 60 m. In jet grouting, cement grout is injected horizontally under high pressure through ports in the sides of a hollow rod lowered into a previously drilled borehole. Jet grouting begins at the bottom of the borehole and proceeds to the top. Rotation of the injection nozzle as the process occurs allows the jet to cut through and hydraulically mix columns of soil up to 2.4 m in diameter. Air or air and water may also be injected to aid in the mixing process. Jet grouting can be performed in any type of inorganic soil to depths limited only by the range of the drilling equipment.

Defining Terms

Selected terms used in this section are compiled below:

Amplification function: A function that describes the ratio of ground surface motion to bedrock motion as a function of frequency.

Attenuation: The rate at which earthquake ground motion decreases with distance.

Backbone curve: The nonlinear stress–strain curve of a monotonically loaded soil.

Blind thrust faults: Faults at depth occurring under anticlinal folds — since they have only subtle surface expression, their seismogenic potential can only be evaluated by indirect means [22]. Blind thrust faults are particularly worrisome because they are hidden, are associated with folded topography in general, including areas of lower and infrequent seismicity, and therefore result in a situation where the potential for an earthquake exists in any area of anticlinal geology, even if there are few or no earthquakes in the historic record. Recent major earthquakes of this type have included the 1980 M_w 7.3 El Asnam (Algeria), 1988 M_w 6.8 Spitak (Armenia), and 1994 M_w 6.7 Northridge (California) events.

Body waves: Vibrational waves transmitted through the body of the Earth, and are of two types: p waves (transmitting energy via dilatational or push–pull motion), and slower s waves (transmitting energy via shear action at right angles to the direction of motion).

Characteristic earthquake: A relatively narrow range of magnitudes at or near the maximum that can be produced by the geometry, mechanical properties, and state of stress of a fault. [56].

Coherence: The similarity of ground motions at different locations. The coherence of ground motions at closely spaced locations is higher than at greater spacings. At a given spacing, the coherence of low-frequency (long wavelength) components is greater than that of high-frequency (short-wavelength) components.

Cyclic mobility: A phenomenon involving accumulation of porewater pressure during cyclic loading in soils for which the residual shear strength is greater than the shear stress required to maintain static equilibrium.

Cyclic resistance ratio (CRR): The ratio of equivalent shear stress amplitude required to trigger liquefaction to the initial vertical effective stress acting on the soil.

Cyclic stress ratio (CSR): The ratio of equivalent shear stress amplitude of an earthquake ground motion to the initial vertical effective stress acting on the soil.

Damping: The force or energy lost in the process of material deformation (damping coefficient c = force per velocity).

Damping curve: A plot of equivalent viscous damping ratio as a function of shear strain amplitude.

Differential settlement: The relative amplitudes of settlement at different locations. Differential settlement may be particularly damaging to bridges and other structures.

Dip: The angle between a plane, such as a fault, and the Earth's surface.

Dip-slip: Motion at right angles to the strike, up- or down-slip.

Ductility factor: The ratio of the total displacement (elastic plus inelastic) to the elastic(i.e., yield) displacement.

Epicenter: The projection on the surface of the Earth directly above the hypocenter.

Equivalent linear analysis: An analysis in which the stress–strain behavior of the soil is characterized by a secant shear modulus and damping ratio that, through a process of iteration, are compatible with the level of shear strain induced in the soil.

Far-field: Beyond near-field, also termed teleseismic.

Fault: A zone of the Earth's crust within which the two sides have moved — faults may be hundreds of miles long, from 1 to over 100 miles deep, and may not be readily apparent on the ground surface.

Flow failure: A soil failure resulting from flow liquefaction. Flow failures can involve very large deformations.

Flow liquefaction: A phenomenon that can occur when liquefaction is triggered in a soil with a residual shear strength lower than the shear stress required to maintain static equilibrium.

Hypocenter: The location of initial radiation of seismic waves (i.e., the first location of dynamic rupture).

Intensity: A metric of the effect, or the strength, of an earthquake hazard at a specific location, commonly measured on qualitative scales such as MMI, MSK, and JMA.

Lateral spreading: A phenomenon resulting from cyclic mobility in soils with some nonzero initial shear stress. Lateral spreading is characterized by the incremental development of permanent lateral soil deformations.

Magnitude: A unique measure of an individual earthquake's release of strain energy, measured on a variety of scales, of which the moment magnitude M_w (derived from seismic moment) is preferred.

Magnitude-frequency relation: The probability of occurrence of a selected magnitude — the commonest is $\log_{10} n(m) = a - bm$ [25]

Meizoseismal: The area of strong shaking and damage.

Modulus reduction curve: The ratio of secant shear modulus at a particular shear strain to maximum shear modulus (corresponding to very low strains) plotted as a function of shear strain amplitude.

Near-field: Within one source dimension of the epicenter, where source dimension refers to the length or width of faulting, whichever is less.

Nonlinear approach: An analysis in which the nonlinear, inelastic stress–strain behavior of the soil is explicitly modeled.

Normal fault: A fault that exhibits dip-slip motion, where the two sides are in tension and move away from each other.

Peak ground acceleration (PGA): The maximum amplitude of recorded acceleration (also termed the ZPA, or zero-period acceleration)

Pseudo-static approach: A method of analysis in which the complex, transient effects of earthquake shaking are represented by constant accelerations. The inertial forces produced by these accelerations are considered, along with the static forces, in limit equilibrium stability analyses.

Radiation damping: A reduction in wave amplitude due to geometric spreading of traveling waves, or radiation into adjacent or underlying materials.

Response spectrum: A plot of maximum amplitudes (acceleration, velocity or displacement) of an sdof oscillator, as the natural period of the SDOF is varied across a spectrum of engineering interest (typically, for natural periods from 0.03 to 3 or more seconds or frequencies of 0.3 to 30+ Hz).

Reverse fault: A fault that exhibits dip-slip motion, where the two sides are in compression and move away toward each other.

Seismic hazards: The phenomena and/or expectation of an earthquake-related agent of damage, such as fault rupture, vibratory ground motion (i.e., shaking), inundation (e.g., tsunami, seiche, dam failure), various kinds of permanent ground failure (e.g., liquefaction), fire or hazardous materials release.

Seismic moment: The moment generated by the forces generated on an earthquake fault during slip.

Seismotectonic model: A mathematical model representing the seismicity, attenuation, and related environment.

Specific impedance: Product of density and wave propagation velocity.

Spectrum amplification factor: The ratio of a response spectral parameter to the ground motion parameter (where parameter indicates acceleration, velocity, or displacement).

Strike: The intersection of a fault and the surface of the Earth, usually measured from the north (e.g., the fault strike is N 60° W).

Strike slip fault: See Transform or Strike slip fault.

Subduction: The plunging of a tectonic plate (e.g., the Pacific) beneath another (e.g., the North American) down into the mantle, due to convergent motion.

Surface waves: Vibrational waves transmitted within the surficial layer of the Earth, of two types: horizontally oscillating Love waves (analogous to S body waves) and vertically oscillating Rayleigh waves.

Thrust fault: Low-angle reverse faulting (blind thrust faults are faults at depth occurring under anticlinal folds — they have only subtle surface expression).

Total settlement: The total amplitude of settlement at a particular location.

Transform or strike slip fault: A fault where relative fault motion occurs in the horizontal plane, parallel to the strike of the fault.

Uniform hazard spectra: Response spectra with the attribute that the probability of exceedance is independent of frequency.

Yield acceleration: The horizontal acceleration that produces a pseudo-static factor of safety of 1. Accelerations greater than the yield acceleration are expected to produce permanent deformations.

References

1. Bartlett, S.F. and Youd, T.L., Empirical analysis of horizontal ground displacement generated by liquefaction-induced lateral spread, *Technical Report NCEER-92-0021*, National Center for Earthquake Engineering Research, Buffalo, NY, 1992.
2. Bell, F.G., *Engineering Treatment of Soils*, E & FN Spon, London, 1993, 302 pp.

3. Bernreuter, D.L. et al., Seismic Hazard Characterization of 69 Nuclear Power Plant Sites East of the Rocky Mountains, U.S. Nuclear Regulatory Commission, NUREG/CR-5250, 1989.
4. Bolt, B.A., *Earthquakes*, W.H. Freeman, New York, 1993.
5. Bonilla, M.G. et al., Statistical relations among earthquake magnitude, surface rupture length, and surface fault displacement, *Bull. Seismol. Soc. Am*., 74(6), 2379–2411, 1984.
6. Boore, D.M., Joyner, W.B., and Fumal, T.E., Estimation of Response Spectra and Peak Acceleration from Western North American Earthquakes: An Interim Report, U.S.G.S Open-File Report 93-509, Menlo Park, CA, 1993.
7. Bozorgnia, Y. and Campbell, K.W., Spectral characteristics of vertical ground motion in the Northridge and other earthquakes, *Proc. 4th U.S. Conf. On Lifeline Earthquake Eng.*, American Society of Civil Engineers, New York, 660–667, 1995.
8. Broms, B., Deep compaction of granular soil, in H.-Y. Fang, Ed., *Foundation Engineering Handbook,* 2nd ed., Van Nostrand Reinhold, New York, 1991, 814–832.
9. BSSC, NEHRP Recommended Provisions for Seismic Regulations for New Buildings, 1994.
10. Campbell, K.W., Strong ground motion attenuation relations: a ten-year perspective, *Earthquake Spectra*, 1(4), 759–804, 1985.
11. Campbell, K.W. and Bozorgnia, Y., Near-source attenuation of peak horizontal acceleration from worldwide accelerograms recorded from 1957 to 1993, *Proc. Fifth U.S. National Conference on Earthquake Engineering,* Earthquake Engineering Research Institute, Oakland, CA, 1994.
12. Clough, R.W. and Penzien, J., *Dynamics of Structures*, McGraw-Hill, New York, 1975.
13. Cornell, C.A., Engineering seismic risk analysis, *Bull. Seismol Soc. Am*., 58(5), 1583–1606, 1968.
14. Cornell, C.A. and Merz, H.A., Seismic risk analysis based on a quadratic magnitude frequency law, *Bull. Seis. Soc. Am*., 63(6), 1992–2006, 1973.
15. Crouse, C. B., Ground-motion attenuation equations for earthquakes on the cascadia subduction zone, *Earthquake Spectra*, 7(2), 201–236, 1991.
16. Darragh, R.B., Huang, M.J., and Shakal, A.F., Earthquake engineering aspects of strong motion data from recent California earthquakes, *Proc. Fifth U.S. National Conf. Earthquake Engineering,* V. III, Earthquake Engineering Research Institute, Oakland, CA, 99–108, 1994.
17. Donovan, N.C. and Bornstein, A.E., Uncertainties in seismic risk procedures, *J. Geotech. Div.*, 104(GT7), 869–887, 1978.
18. EduPro Civil Systems, Inc., *ProShake User's Manual*, EduPro Civil Systems, Inc., Redmond, WA, 1998, 52 pp.
19. Electric Power Research Institute, Seismic Hazard Methodology for the Central and Eastern United States, EPRI NP-4726, Menlo Park, 1986.
20. Esteva, L., Seismicity, in *Seismic Risk and Engineering Decisions,* Lomnitz, C. and Rosenblueth, E., Eds., Elsevier, New York, 1976.
21. Finn, W.D.L., Yogendrakumar, M., Yoshida, M., and Yoshida, N., TARA-3: A program to compute the response of 2-D embankments and soil-structure interaction systems to seismic loadings, Department of Civil Engineering, University of Brirish Columbia, Vancouver, Canada, 1986.
22. Greenwood, R.B., Characterizing blind thrust fault sources — an overview, in Woods, M.C. and Seiple. W.R., Eds., The Northridge California Earthquake of 17 January 1994, California Department Conservation, Division of Mines and Geology, Special Publ. 116, 1995, 279–287.
23. Gumbel, E.J., *Statistics of Extremes,* Columbia University Press, New York, 1958.
24. Gutenberg, B. and Richter, C.F., *Seismicity of the Earth and Associated Phenomena*, Princeton University Press, Princeton, NJ, 1954.
25. Gutenberg, B. and Richter, C. F., Magnitude and energy of earthquakes, *Ann. Geof.*, 9(1), p 1–15, 1956.
26. Hanks, T.C. and Kanamori, H., A moment magnitude scale, *J. Geophys. Res*., 84, 2348–2350, 1979.
27. Hausmann, M.R., *Engineering Principles of Ground Modification*, McGraw-Hill, New York, 1990, 632 pp.

28. Housner, G., Historical view of earthquake engineering, in *Proc. Post-Conf. Volume, Eighth World Conf. on Earthquake Engineering,* Earthquake Engineering Research Institute, Oakland, CA, 1984, 25–39, as quoted by S. Otani [1995].
29. Kagawa, T., Mejia, L., Seed, H.B., and Lysmer, J., TLUSH — a computer program for three-dimensional dynamic analysis of Earth dams, Report No. UCB/EERC-81/14, University of California, Berkeley, 1981.
30. Lawson, A. C. and Reid, H.F., *The California Earthquake of April 18, 1906. Report of the State Earthquake Investigation Commission,* California. State Earthquake Investigation Commission, Carnegie Institution of Washington, Washington, D.C., 1908–1910.
31. Lee, M.K.W and Finn, W.D.L., DESRA-2, Dynamic effective stress response analysis of soil deposits with energy transmitting boundary including assessment of liquefaction potential, Soil Mechanics Series No. 38, University of British Columbia, Vancouver, 1978.
32. Liao, S.S.C., Veneziano, D., and Whitman, R.V., Regression models for evaluating liquefaction probability, *J. Geotech. Eng. ASCE,* 114(4), 389–411, 1988.
33. Lomnitz, C., *Global Tectonics and Earthquake Risk*, Elsevier, New York, 1974.
34. Lysmer, J., Udaka, T., Tsai, C.F., and Seed, H.B., FLUSH — A computer program for approximate 3-D analysis of soil-structure interaction problems, Report No. EERC 75-30, Earthquake Engineering Research Center, University of California, Berkeley, 1975, 83 pp.
35. MacMurdo, J., Papers relating to the earthquake which occurred in India in 1819, *Philos. Mag.,* 63, 105–177, 1824.
36. Makdisi, F.I. and Seed, H.B., Simplified procedure for estimating dam and embankment earthquake-induced deformations, *J. Geotech. Eng. Div. ASCE,* 104(GT7), 849–867, 1978.
37. McGuire, R. K., FRISK: Computer Program for Seismic Risk Analysis Using Faults as Earthquake Sources. U.S. Geological Survey, Reports, U.S. Geological Survey Open file 78-1007, 1978, 71 pp.
38. Meeting on Updating of MSK-64, Report on the ad hoc Panel Meeting of Experts on Updating of the MSK-64 Seismic Intensity Scale, Jene, 10–14 March 1980, *Gerlands Beitr. Geophys*., Leipzeig 90(3), 261–268, 1981.
39. Mitchell, J.K. and Tseng, D.-J., Assessment of liquefaction potential by cone penetration resistance, *Proceedings, H. Bolton Seed Memorial Symposium,* Berkeley, CA, Vol. 2, J.M. Duncan, Ed., 1990, 335–350.
40. Mononobe, N. and Matsuo, H., On the determination of Earth pressures during earthquakes, *Proceedings, World Engineering Congress,* 9, 1929.
41. Mosely, M.P., ed., *Ground Improvement*, Blackie Academic & Professional, London, 1993, 218 pp.
42. National Academy Press, *Probabilistic Seismic Hazard Analysis*, National Academy of Sciences, Washington, D.C., 1988.
43. Newmark, N., Effects of earthquakes on dams and embankments, *Geotechnique*, 15(2), 139–160, 1965.
44. Ohsaki, Y., Effects of sand compaction on liquefaction during Tokachioki earthquake, *Soils Found.,* 10(2), 112–128, 1970.
45. Okabe, S., General theory of Earth pressures, *J. Jpn. Soc. Civil Eng.*, 12(1), 1926.
46. Olson, R.S., Cyclic liquefaction based on the cone penetrometer test, Proceedings of the NCEER Workshop on Evaluation of Liquefaction Resistance of Soils, Technical Report NCEER-97-0022, T.L. Youd and I.M. Idriss, Eds., National Center for Earthquake Engineering Research, Buffalo, NY, 1997, 280 pp.
47. Pyke, R., Seed, H.B., and Chan, C.K., Settlement of sands under multi-directional loading, *J. Geotech. Eng. Div. ASCE,* 101(GT4), 379–398, 1975.
48. Pyke, R.L., TESS1 User's Guide, TAGA Engineering Software Services, Berkeley, CA, 1985.
49. Reid, H.F., The Mechanics of the Earthquake, The California Earthquake of April 18, 1906, Report of the State Investigation Committee, vol. 2, Carnegie Institution of Washington, Washington, D.C., 1910.

50. Reiter, L., *Earthquake Hazard Analysis, Issues and Insights*, Columbia University Press, New York, 1990.
51. Richter, C. F., An instrumental earthquake scale, *Bull. Seismol. Soc. Am.*, 25 1–32, 1935.
52. Richter, C.F., *Elementary Seismology*, W.H. Freeman, San Francisco, 1958.
53. Schnabel, P.B., Lysmer, J., and Seed, H.B., SHAKE: A computer program for earthquake response analysis of horizontally layered sites, Report No. EERC 72-12, Earthquake Engineering Research Center, University of California, Berkeley, 1972.
54. Scholz, C.H., *The Mechanics of Earthquakes and Faulting*, Cambridge University Press, New York, 1990.
55. Schwartz, D.P., Geologic characterization of seismic sources: moving into the 1990s, in *Earthquake Engineering and Soil Dynamics II — Recent Advances in Ground-Motion Evaluation*, J.L. v. Thun, Ed., Geotechnical Spec. Publ. No. 20., American Society of Civil Engineers, New York, 1988.
56. Schwartz, D.P. and Coppersmith, K.J., Fault behavior and characteristic earthquakes: examples from the Wasatch and San Andreas faults, *J. Geophys. Res.*, 89, 5681–5698, 1984.
57. Seed, H.B. and De Alba, P., Use of SPT and CPT tests for evaluating the liquefaction resistance of soils, *Proceedings, Insitu '86,* ASCE, 1986.
58. Seed, H.B. and Silver, M.L., Settlement of dry sands during earthquakes, *J. Soil Mech. Found. Div.*, 98(SM4), 381–397, 1972.
59. Seed, H.B., Ugas, C., and Lysmer, J., Site-dependent spectra for earthquake-resistant design, *Bull. Seismol. Soc. Am.*, 66, 221–243, 1976.
60. Slemmons, D.B., State-of-the-art for assessing earthquake hazards in the United States, Report 6: Faults and earthquake magnitude, U.S. Army Corps of Engineers, Waterways Experiment Station, Misc. Paper s-73-1, 1977, 129 pp.
61. Stein, R.S. and Yeats, R.S., Hidden earthquakes, *Sci. Am.*, June, 1989.
62. Stokoe, K.H. II, Roesset, J.M., Bierschwale, J.G., and Aouad, M., Liquefaction potential of sands from shear wave velocity, *Proceedings, 9th World Conference on Earthquake Engineering,* Tokyo, Japan, Vol. 3, 1988, 213–218.
63. Tokimatsu, K. and Seed, H.B., Evaluation of settlements in sand due to earthquake shaking, *J. Geotechn. Eng. ASCE,* 113(8), 861–878, 1987.
64. Tokimatsu, K., Kuwayama, S., and Tamura, S., Liquefaction potential evaluation based on Rayleigh wave investigation and its comparison with field behavior, *Proceedings, 2nd International Conference on Recent Advances in Geotechnical Earthquake Engineering and Soil Dynamics,* St. Louis, MO, Vol. 1, 1991, 357–364.
65. Van Impe, W.F., *Soil Improvement Techniques and Their Evolution*, A.A. Balkema, Rotterdam, 1989, 125 pp.
66. Wells, D.L. and Coppersmith, K.J., Empirical relationships among magnitude, rupture length, rupture width, rupture area and surface displacement, *Bull. Seisinol. Soc. Am.*, 84(4), 974–1002, 1994.
67. Welsh, J.P., Soil Improvement: A Ten Year Update, Geotechnical Special Publication No. 12, ASCE, New York, 1987, 331 pp.
68. Wood, H.O. and Neumann, Fr., Modified Mercalli intensity scale of 1931, *Bull. Seismol. Soc. Am.*, 21, 277–283, 1931.
69. Wood, J., Earthquake-Induced Soil Pressures on Structures, Report No. EERL 73-05, California Institute of Technology, Pasadena, 1973, 311 pp.
70. Yegulalp, T.M. and Kuo, J.T., Statistical prediction of the occurrence of maximum magnitude earthquakes, *Bull. Seis. Soc. Am.*, 64(2), 393–414, 1974.
71. Youngs, R R. and Coppersmith, K J., Attenuation relationships for evaluation of seismic hazards from large subduction zone earthquakes, *Proceedings of Conference XLVIII: 3rd Annual Workshop on Earthquake Hazards in the Puget Sound, Portland Area*, March 28–30, 1989, Portland, OR; Hays-Walter-W., Ed., U.S. Geological Survey, Reston, VA, 1989, 42–49.
72. Youngs, R.R. and Coppersmith, K.J., Implication of fault slip rates and earthquake recurrence models to probabilistic seismic hazard estimates, *Bull. Seismol. Soc. Am.*, 75, 939–964, 1987.